The Astronomical Journal, 161:235 (16pp), 2021 May https://doi.org/10.3847/1538-3881/abeaa1

A Transiting Warm Giant Planet around the Young Active Star TOI-201

Melissa J. Hobson[1,2], Rafael Brahm[1,3], Andrés Jordán[1,3], Nestor Espinoza[4], Diana Kossakowski[5], Thomas Henning[5], Felipe Rojas[1,2], Martin Schlecker[5], Paula Sarkis[5], Trifon Trifonov[5], Daniel Thorngren[6], Avraham Binnenfeld[7], Sahar Shahaf[8], Shay Zucker[7], George R. Ricker[9], David W. Latham[10], S. Seager[9,11,12], Joshua N. Winn[13], Jon M. Jenkins[14], Brett Addison[15], François Bouchy[16], Brendan P. Bowler[17], Joshua T. Briegal[18], Edward M. Bryant[19,20], Karen A. Collins[10], Tansu Daylan[9,31], Nolan Grieves[16], Jonathan Horner[15], Chelsea Huang[9], Stephen R. Kane[21], John Kielkopf[22], Brian McLean[23], Matthew W. Mengel[15], Louise D. Nielsen[16], Jack Okumura[15], Matias Jones[24,25], Peter Plavchan[26], Avi Shporer[9], Alexis M. S. Smith[27], Rosanna Tilbrook[28], C. G. Tinney[29], Joseph D. Twicken[14,30], Stéphane Udry[16], Nicolas Unger[16], Richard West[19], Robert A. Wittenmyer[15], Bill Wohler[14,30], Pascal Torres[1,2], and Duncan J. Wright[15]

[1] Millennium Institute for Astrophysics, Chile; mhobson@astro.puc.cl
[2] Instituto de Astrofísica, Facultad de Física, Pontificia Universidad Católica de Chile, Av. Vicuña Mackenna 4860, 782-0436 Macul, Santiago, Chile
[3] Facultad de Ingeniería y Ciencias, Universidad Adolfo Ibáñez, Av. Diagonal las Torres 2640, Peñalolén, Santiago, Chile
[4] Space Telescope Science Institute, 3700 San Martin Drive, Baltimore, MD 21218, USA
[5] Max-Planck-Institut für Astronomie, Königstuhl 17, D-69117 Heidelberg, Germany
[6] University of Montréal, Montréal, QC, Canada
[7] Porter School of the Environment and Earth Sciences, Raymond and Beverly Sackler Faculty of Exact Sciences, Tel Aviv University, Tel Aviv, 6997801, Israel
[8] School of Physics and Astronomy, Raymond and Beverly Sackler Faculty of Exact Sciences, Tel Aviv University, Tel Aviv, 6997801, Israel
[9] Department of Physics and Kavli Institute for Astrophysics and Space Research, Massachusetts Institute of Technology, Cambridge, MA 02139, USA
[10] Center for Astrophysics, Harvard & Smithsonian, 60 Garden Street, Cambridge, MA 02138, USA
[11] Department of Earth, Atmospheric and Planetary Sciences, Massachusetts Institute of Technology, Cambridge, MA 02139, USA
[12] Department of Aeronautics and Astronautics, MIT, 77 Massachusetts Avenue, Cambridge, MA 02139, USA
[13] Department of Astrophysical Sciences, Princeton University, 4 Ivy Lane, Princeton, NJ 08544, USA
[14] NASA Ames Research Center, Moffett Field, CA 94035, USA
[15] University of Southern Queensland, Centre for Astrophysics, West Street, Toowoomba, QLD 4350, Australia
[16] Geneva Observatory, University of Geneva, Chemin des Mailettes 51, 1290 Versoix, Switzerland
[17] Department of Astronomy, The University of Texas at Austin, TX 78712, USA
[18] Astrophysics Group, Cavendish Laboratory, J.J. Thomson Avenue, Cambridge CB3 0HE, UK
[19] Department of Physics, University of Warwick, Gibbet Hill Road, Coventry CV4 7AL, UK
[20] Centre for Exoplanets and Habitability, University of Warwick, Gibbet Hill Road, Coventry CV4 7AL, UK
[21] Department of Earth and Planetary Sciences, University of California, Riverside, CA 92521, USA
[22] Department of Physics and Astronomy, University of Louisville, Louisville, KY 40292, USA
[23] Space Telescope Science Institute, Mikulski Archive for Space Telescopes, Baltimore, MD 21218, USA
[24] European Southern Observatory, Alonso de Córdova 3107, Santiago, Chile
[25] Instituto de Astronomía, Universidad Católica del Norte, Angamos 0610, 1270709, Antofagasta, Chile
[26] George Mason University, 4400 University Drive MS 3F3, Fairfax, VA 22030, USA
[27] Institute of Planetary Research, German Aerospace Center, Rutherfordstrasse 2, D-12489, Berlin, Germany
[28] School of Physics and Astronomy, University of Leicester, University Road, Leicester LE1 7RH, UK
[29] Exoplanetary Science at UNSW, School of Physics, UNSW Sydney, NSW 2052, Australia
[30] SETI Institute, Mountain View, CA 94043, USA
Received 2020 November 25; revised 2021 February 19; accepted 2021 February 26; published 2021 April 26

Abstract

We present the confirmation of the eccentric warm giant planet TOI-201 b, first identified as a candidate in Transiting Exoplanet Survey Satellite photometry (Sectors 1–8, 10–13, and 27–28) and confirmed using ground-based photometry from Next Generation Transit Survey and radial velocities from FEROS, HARPS, CORALIE, and MINERVA-Australis. TOI-201 b orbits a young ($0.87^{+0.46}_{-0.49}$ Gyr) and bright ($V = 9.07$ mag) F-type star with a 52.9781 day period. The planet has a mass of $0.42^{+0.05}_{-0.03}\,M_{\rm J}$, a radius of $1.008^{+0.012}_{-0.015}\,R_{\rm J}$, and an orbital eccentricity of $0.28^{+0.06}_{-0.09}$; it appears to still be undergoing fairly rapid cooling, as expected given the youth of the host star. The star also shows long-term variability in both the radial velocities and several activity indicators, which we attribute to stellar activity. The discovery and characterization of warm giant planets such as TOI-201 b are important for constraining formation and evolution theories for giant planets.

Unified Astronomy Thesaurus concepts: Exoplanet astronomy (486); Exoplanet detection methods (489); Transit photometry (1709); Radial velocity (1332)

1. Introduction

Transiting warm giants—that is, planets with $R_P \gtrsim 0.8\,R_{\rm J}$ and $10\,{\rm days} \lesssim P \lesssim 100\,{\rm days}$—are particularly important for understanding the formation and evolution of giant planets. Unlike hot Jupiters—i.e., planets with $R_P \gtrsim 0.8\,R_{\rm J}$ and $P \lesssim 10$ days—which are inflated by mechanisms that are still unclear but likely connected to irradiation (e.g., Sarkis et al. 2021), these more distant planets are less strongly irradiated by their host star, meaning their size and mass can be effectively modeled by their metallicity (e.g., Thorngren & Fortney 2019). Both hot and warm Jupiters are unlikely to form in situ, but rather are expected to have formed in the outer regions of the disk and migrated to their

[31] Kavli Fellow.

current locations; the main mechanisms proposed are gas-disk migration and high-eccentricity migration (see Dawson & Johnson 2018 for a comprehensive review). However, hot Jupiters' orbital histories are affected by tidal evolution, which can erase traces of past interactions between planets; this is not the case for warm Jupiters. Therefore, this population of planets preserves valuable information for the study of giant planet formation in their physical and orbital parameters. These parameters can be characterized through the combination of photometry and radial velocities.

While the current sample of warm giants is still small, the Transiting Exoplanet Survey Satellite (TESS; Ricker et al. 2015) is expected to detect hundreds of such planets (Sullivan et al. 2015; Barclay et al. 2018). The Warm gIaNts with tEss collaboration (WINE; e.g., Brahm et al. 2019; Jordán et al. 2020) is using a network of photometric and spectroscopic facilities to follow up, confirm, and characterize warm giant candidates from TESS. One such candidate is TOI-201.01.

In this paper, we present the confirmation and characterization of the warm giant TOI-201 b, orbiting the young F-type star TOI-201. The paper is organized as follows. We present the observational data in Section 2. In Section 3 we analyze the data, and characterize the star and planet. Finally, our results are discussed in Section 4.

2. Observations

2.1. Photometric Data

2.1.1. TESS

TOI-201 was observed by the TESS mission between 2018 July 25 and 2019 July 17, in Sectors 1, 2, 3, 4, 5, 6, 7, 8, 10, 11, 12, and 13, using camera 4. CCD 1 was used for Sectors 3, 4, and 5, CCD 2 for Sectors 6, 7, and 8, CCD 3 for Sectors 10, 11, and 12, and CCD 4 for Sectors 1, 2, and 13. Currently, it is also being observed as part of the extended mission; the light curves from Sectors 27 and 28, which were observed between 2020 July 5 and August 25, were also incorporated into the analysis. Camera 4 in CCD 4 was used for both these Sectors.

The 2 minute cadence data for TOI-201 were processed in the TESS Science Processing Operation Center (SPOC; Jenkins et al. 2016) pipeline. Two potential transit signals were identified in the SPOC transit search (Jenkins 2002; Jenkins et al. 2010, 2020) of the TOI-201 light curve. These were designated as TESS Objects of Interest (TOIs) by the TESS Science Office based on SPOC data validation results (Twicken et al. 2018; Li et al. 2019) indicating that both signals were consistent with transiting planets. The planetary candidates are listed in the ExoFOP-TESS archive[32]: TOI-201.01, with a period of $P_{01} = 52.978306$ days, and TOI-201.02, with a period of $P_{02} = 5.849173$ days. The full PDCSAP light curve (Smith et al. 2012; Stumpe et al. 2012, 2014), obtained from the MAST archive, is shown in Figure 1 (top panel). Any points that were flagged as being of low quality have been removed. Six full transits of TOI-201.01 are clearly visible, in Sectors 2, 4, 6, 10, 12, and 28. A partial transit is also visible in Sector 8, at the edge of a five day gap in the light curve (Figure 1, bottom panel). This gap is due to an instrument turn-off between TJD[33] 1531.74 and TJD 1535.00, caused by an interruption in communications between the instrument and spacecraft. The flux is clearly overestimated for the first ∼0.5 days after the gap. This artifact appears to have been introduced in the SPOC PDC processing, as the SAP light curve shows a low flux level for this period, which is likely due to the camera temperature change of ∼20° during the instrument turn-off, as detailed in the TESS Data Release Notes for Sector 8, DR10.[34] The transits of TOI-201.02 have a much shallower depth (only 0.128 ± 0.013 mmag, compared to 6.843 ± 0.058 mmag for TOI-201.01), and are hence not visually obvious in the light curve.

2.1.2. Next Generation Transit Survey

Due to the relatively large 21″ pixel size of TESS, nearby companions can contaminate its photometry. It is therefore necessary to identify possible contaminating sources, which can create false positives or dilute the transits. Ground-based photometry plays an important role in disentangling these false positives. In this context, The Next Generation Transit Survey (NGTS; Wheatley et al. 2018) observed TOI-201 on 2019 September 19, obtaining a clear ingress signal (Figure 2). Two telescopes were used, with the custom NGTS filter (520–890 nm). A total of 2484 images were obtained with an exposure time of 10 s, for an overall cadence (exposure, read out, etc.) of 13 s. The images were reduced with a custom aperture photometry pipeline (Bryant et al. 2020), using an aperture with a radius of 7 pixels (35″).

2.2. High-resolution Imaging

High-resolution imaging is a valuable tool for rejecting false-positive scenarios for TESS candidates. In this context, the Southern Astrophysical Research (SOAR) TESS survey (Ziegler et al. 2020) has observed TESS planet candidate hosts with speckle imaging using the high-resolution camera (HRCam) imager on the 4.1 m SOAR telescope at Cerro Pachón, Chile (Tokovinin 2018). TOI-201 was observed on the night of 2019 February 18, with no nearby sources detected within 3″. The contrast curve and auto-correlation function are shown in Figure 3.

2.3. Spectroscopic Data

The WINE consortium carried out spectroscopic follow-up of TOI-201 with the FEROS and HARPS spectrographs. In addition to these, we also obtained data from the CORALIE and MINERVA-Australis teams. Finally, TOI-201 was observed once with the Network of Robotic Echelle Spectrographs (NRES), for the purpose of stellar parameter determination.

2.3.1. FEROS

We obtained 52 spectra with the FEROS spectrograph (Kaufer et al. 1999), which is mounted on the MPG 2.2 m telescope at La Silla Observatory and has a resolving power of $R = 50{,}000$, between 2018 November 26 and 2020 March 8. The observations were performed in the Object-Calibration mode, with an exposure time of 5 minutes. The spectra, which have a median signal-to-noise ratio (S/N) of 165, were processed with the CERES pipeline (Brahm et al. 2017a). From this pipeline, we obtain both radial velocities (RVs) and activity indicators. Specifically, we compute the bisector of the CCF (BIS), which traces photospheric activity

[32] Located at https://exofop.ipac.caltech.edu/tess/target.php?id=350618622.
[33] TESS Julian Date, TJD = BJD–2457000.0.
[34] Archived at https://archive.stsci.edu/missions/tess/doc/tess_drn/tess_sector_08_drn10_v02.pdf.

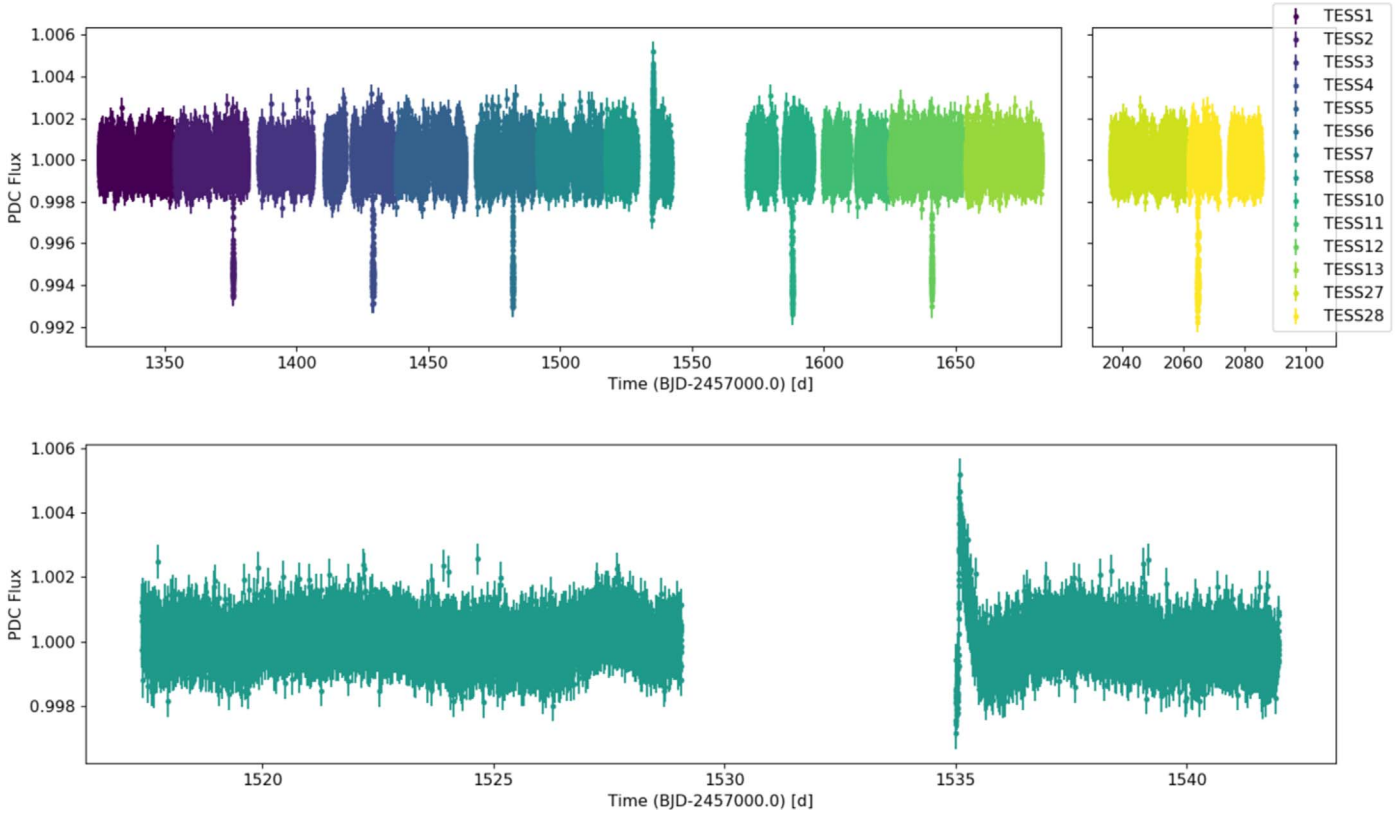

Figure 1. Top: Transiting Exoplanet Survey Satellite (TESS) light curve for TOI-201, for all Sectors. The data are color-coded by Sectors, and flagged points have been removed. The left subplot shows the 12 Sectors from the prime mission, and the right subplot the two Sectors from the extended mission. Bottom: zoom to Sector 8, showing the five day gap in the light curve, and the partial transit of TOI-201.01 at the edge of the gap.

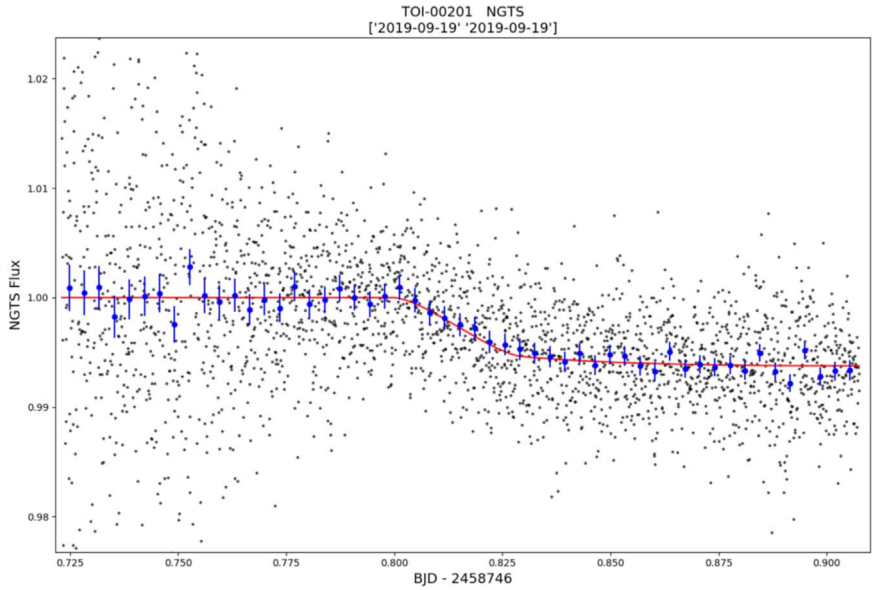

Figure 2. Next Generation Transit Survey light curve for TOI-201, observed on 2019 September 19. The blue points show the data binned to 5 minutes. The red line indicates the predicted model from the TESS data, using ephemeris of $T_0 = 1376.052045$, $P = 52.978306$ days.

(e.g., Queloz et al. 2001a), and the H_α, $\log(R'_{HK})$, Na II, and He I activity indices, which trace chromospheric activity. For H_α, we used the definition of Boisse et al. (2009). As TOI-201 is an F-type star, we used the regions defined by Duncan et al. (1991) and the calibrations of Noyes et al. (1984) for $\log(R'_{HK})$. For Na II and He I we followed Gomes da Silva et al. (2011). The radial velocities and activity indices computed from the FEROS data are listed in Table A1; the RVs have a median error of $\sigma_{RV} \approx 9.1\ m\ s^{-1}$.

2.3.2. HARPS

We obtained 39 spectra with the HARPS spectrograph (Mayor et al. 2003), which is mounted on the 3.6 m telescope at La Silla

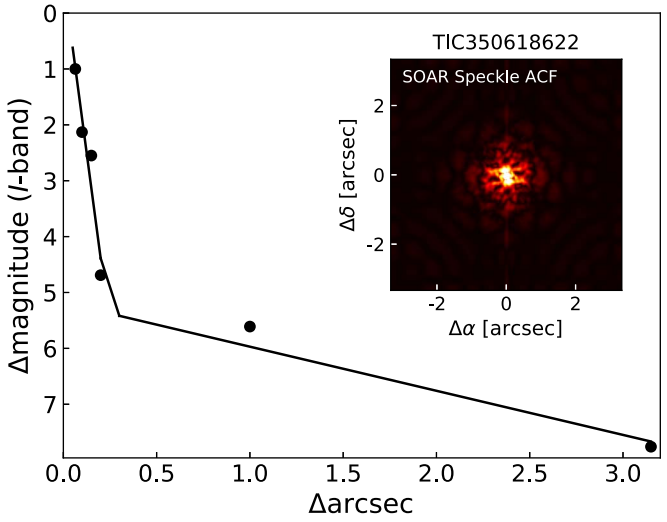

Figure 3. Contrast curve and speckle auto-correlation function from the high-resolution camera at Southern Astrophysical Research (SOAR) for TOI-201. The black points and solid line indicate the 5σ contrast curve; the inset shows the speckle auto-correlation function.

Observatory, and has a resolving power of $R = 120{,}000$. The spectra were obtained between 2018 December 11 and 2020 February 21, under Program IDs 0101.C-0510(D), 0102.C-0451(B), 0103.C-0442(A), and 0104.C-0413(A). The exposures were taken in simultaneous sky mode, with a 10 minute duration. One observation, obtained on 2020 January 17, has an extremely low S/N of 17 and was therefore removed from the analysis. The remaining 38 spectra have a median S/N of 109. As with the FEROS spectra, we processed the HARPS spectra using the CERES pipeline, obtaining the RVs and the same set of activity indicators. The RVs and activity indices computed from the HARPS data are listed in Table A2; the RVs have a median error of $\sigma_{\rm RV} \approx 2.0\,{\rm m\,s^{-1}}$.

2.3.3. CORALIE

A total of 10 spectra of TOI-201 were obtained with the CORALIE high-resolution spectrograph on the Swiss 1.2 m Euler telescope at La Silla Observatory, Chile (Queloz et al. 2001b), between 2018 November 12 and 2019 March 27. Each exposure had a duration of 20 minutes yielding an S/N of ∼45. CORALIE is a fiber-fed echelle spectrograph with a 2″ science fiber and a secondary fiber with a Fabry–Perot for simultaneous wavelength calibration. We extracted RV measurements by cross-correlation of the spectra with a binary G2V template (Baranne et al. 1996; Pepe et al. 2002). We obtained final RV uncertainties for the CORALIE epochs of $\sigma_{\rm RV} \approx 10$–$15\,{\rm m\,s^{-1}}$. BIS, FWHM and other line-profile diagnostics were computed as well using the standard CORALIE DRS. We also computed the H_α index for each spectrum to check for possible variation in stellar activity. We investigated various scenarios where a blended eclipsing stellar binary can mimic a transiting planet using the line profile diagnostics and found no evidence of such.

2.3.4. MINERVA-Australis

MINERVA-Australis is an array of four PlaneWave CDK700 telescopes located in Queensland, Australia, fully dedicated to the precise RV follow-up of TESS candidates (e.g., Addison et al. 2020, 2021; Jordán et al. 2020). The four telescopes can be simultaneously fiber-fed to a single KiwiSpec R4-100 high-resolution ($R = 80{,}000$) spectrograph (Barnes et al. 2012; Addison et al. 2019). We obtained 62 spectra of TOI-201 in the early days of MINERVA-Australis, with a single telescope, between 2019 January 2 and April 15. Exposure times were 30 minutes, and on some nights, two consecutive exposures were obtained. The resulting RVs are given in Table A4. RVs for the observations are derived for each telescope by cross-correlation, where the template being matched is the mean spectrum of each telescope. The instrumental variations are corrected by using simultaneous thorium–argon arc lamp observations.

2.3.5. NRES

The NRES (Siverd et al. 2018) of the Las Cumbres Observatory (Brown et al. 2013) consists of four identical fiber-fed optical echelle spectrographs, with a resolving power of $R \approx 53{,}000$, mounted on globally distributed 1 m telescopes. TOI-201 was observed by NRES at CTIO on 2018 December 8. A SpecMatch analysis (Yee et al. 2017) was performed on the spectrum, yielding the following stellar parameters: $T_{\rm eff} = 6280 \pm 100$ K, $\log g = 4.3 \pm 0.1$, ${\rm Fe/H} = 0.21 \pm 0.06$, $v \sin i = 8.4 \pm 2.1\,{\rm km\,s^{-1}}$, $M_\star = 1.285 \pm 0.064\,M_\odot$, and $R_\star = 1.35 \pm 0.17\,R_\odot$.

3. Analysis

3.1. Stellar Parameters

In order to characterize the host star, we first used the co-added HARPS spectra to determine the atmospheric parameters. We employed the ZASPE code (Brahm et al. 2017b), which compares the observed spectrum to a grid of synthetic models generated from the ATLAS9 model atmospheres (Castelli & Kurucz 2003) in order to determine the effective temperature $T_{\rm eff}$, surface gravity $\log g$, metallicity [Fe/H], and projected rotational velocity $v \sin i$.

Next, we followed the second procedure described in Brahm et al. (2019) to determine the physical parameters. To summarize, we compare the broadband photometric measurements, converted to absolute magnitudes using the Gaia DR2 (Gaia Collaboration et al. 2016, 2018) parallax, with the stellar evolutionary models of Bressan et al. (2012). We use the emcee package (Foreman-Mackey et al. 2013) to sample the posterior distributions. Through this procedure, we determine the age, mass, radius, luminosity, density, and extinction. We also obtain new values for $T_{\rm eff}$ and $\log g$, the last of which is more precise than the one previously determined through ZASPE. Therefore, we iterated the entire procedure, using the new $\log g$ as an additional input parameter for ZASPE. One iteration was sufficient for the $\log g$ value to converge. The stellar parameters and observational properties of TOI-201 are presented in Table 1. The quoted error bars for the stellar parameters are internal errors, computed as the $\pm 1\sigma$ interval around the median of the posterior for each parameter; they do not take into account any systematic errors on the stellar models. The parameters we derive are consistent at 1σ with those obtained from the NRES spectrum (Section 2.3.5). We find that TOI-201 is a young F-type star.

3.2. RV Analysis

In this section, we present the analysis of the FEROS and HARPS spectra, all of which were processed using the CERES pipeline. For homogeneity, we do not include the CORALIE

Table 1
Stellar Parameters of TOI-201

Parameter	Value	Reference
Names	HD 39474	
	TIC 350618622, TOI-201	TESS
	J05493641-5454386	2MASS
	4767547667180525696	Gaia DR2
R.A. (J2000)	$05^{h}49^{m}36\overset{s}{.}4138946584$	Gaia DR2
Decl. (J2000)	$-54^{h}54^{m}38\overset{s}{.}552783926$	Gaia DR2
$pm^{R.A.}$ (mas yr^{-1})	7.731 ± 0.052	Gaia DR2
$pm^{decl.}$ (mas yr^{-1})	66.448 ± 0.058	Gaia DR2
π (mas)	8.7566 ± 0.0265	Gaia DR2
T (mag)	8.5822 ± 0.006	TESS
B (mag)	10.104 ± 0.055	APASS
V (mag)	9.715 ± 0.079	APASS
J (mag)	8.103 ± 0.029	2MASS
H (mag)	7.923 ± 0.036	2MASS
K_s (mag)	7.846 ± 0.024	2MASS
$T_{\rm eff}$ (K)	6394 ± 75	this work
Spectral type	F6V	PM13
Fe/H (dex)	0.240 ± 0.036	this work
$\log g$ (dex)	4.318 ± 0.014	this work
$v \sin i$ (km s^{-1})	9.52 ± 0.278	this work
$R_\star$ ($R_\odot$)	1.317 ± 0.011	this work
$M_\star$ ($M_\odot$)	1.316 ± 0.027	this work
$L_\star$ ($L_\odot$)	2.6 ± 0.1	this work
$\rho_\star$ (g cm^{-3})	0.81 ± 0.03	this work
Age (yr)	$0.87^{+0.46}_{-0.49}$	this work
A_V (mag)	0.11 ± 0.05	this work
$\log R'_{\rm hk}$	-4.76 ± 0.04	this work

Note. TESS: TESS Input Catalog (Stassun 2019); 2MASS: Two-micron All Sky Survey (Skrutskie et al. 2006); Gaia DR2: Gaia Data Release 2 (Gaia Collaboration et al. 2016, 2018); APASS: AAVSO Photometric All-Sky Survey (Munari et al. 2014); PM13: using the tables of Pecaut & Mamajek (2013).

and MINERVA-Australis data in this section, as they were processed using the respective instrument pipelines. Additionally, the FEROS and HARPS data have longer temporal baselines, covering both the 2018–2019 and 2019–2020 observing seasons, whereas CORALIE and MINERVA-Australis only observed TOI-201 during the 2018–2019 season.

The generalized Lomb–Scargle (GLS) periodograms of the joint FEROS and HARPS RV and activity indices time series are presented in Figure 4. The 52.9 day period of the planetary candidate TOI-201.01 is highlighted. There is a clear, highly significant peak close to this period in the RV periodogram, as well as several significant long-period peaks. We do not find significant peaks close to ∼53 days for any of the activity indices, indicating that the signal in the RVs is likely to be planetary in nature. On the other hand, there are several short- and long-term signatures in the activity indices. There is no clear rotation period in the light curve according to Canto Martins et al. (2020), but given the radius and $v \sin i$ reported in Table 1, we may expect a period of ∼7 days (assuming no misalignment); there is a peak at ∼8 days in the RVs, and hints of peaks at the same period in the $\log(R'_{\rm HK})$ Na II and He I periodograms. There are also long-period peaks at ∼300 days in both the H_α and $\log(R'_{\rm HK})$ periodograms, similar to that seen in the RVs. Additionally, there are peaks at ∼40 days in the Na II and He I periodograms, with no obvious correspondence in the RVs.

Correlations between the bisector spans and the RVs can also indicate a stellar origin for radial velocity variations (e.g., Queloz et al. 2001a). The RV measurements are plotted against the bisector spans in Figure 5 for both FEROS and HARPS data. Spearman correlation tests indicate no significant correlation between the bisector spans and the radial velocities, nor between the bisector spans and the orbital phases of TOI-201.01, for either data set. For FEROS, we find a Spearman correlation coefficient $r_s = -0.31$ with p-value $= 0.03$ between the RVs and bisector spans, and $r_s = -0.02$ with p-value $= 0.09$ between the orbital phases and bisector spans; for HARPS, we find $r_s = 0.15$ with p-value $= 0.38$ between the RVs and bisector spans, and $r_s = -0.13$ with p-value $= 0.44$ between the orbital phases and bisector spans.

In order to further verify that the ∼53 day signal is planetary in nature, we also computed the Phase Distance Correlation (PDC) periodogram (Zucker 2018) for the FEROS data. We find a stronger signal at the 53 day period in the PDC periodogram than in a comparison GLS periodogram, as expected for eccentric orbits, as shown in Figure 6. We also ran the recent PDC extension, the USuRPER (Binnenfeld et al. 2020), which is designed to account for fluctuations in the entire spectral shape. A prominent peak is visible in the USuRPER low-frequency region (Figure 6). This result strengthens the finding that those signals are caused by some sort of periodic variation in the spectral feature shape. Both the PDC and USuRPER periodograms are implemented in the SPARTA code library (Shahaf et al. 2020).

We use the `juliet` python package (Espinoza et al. 2019) to model the joint FEROS and HARPS RVs. This tool allows us to jointly fit photometric data (using the `batman` package; Kreidberg 2015) and RVs (using the `radvel` package, Fulton et al. 2018), and also to incorporate Gaussian processes (GPs) (via the `celerite` package; Foreman-Mackey et al. 2017). The parameter space is explored through nested sampling, using the `MultiNest` algorithm (Feroz et al. 2009) in its python implementation, `PyMultiNest` (Buchner et al. 2014), or the `dynesty` package (Speagle 2020).

We tested six models for the radial velocities: a flat model with no Keplerian components; a single circular planet; a single eccentric planet; two eccentric planets; a single eccentric planet plus a quadratic trend to model long-term effects; and a single eccentric planet plus a GP to account for stellar activity. The full priors for each model are listed in Table 2, and the posteriors in Table 3. For all Keplerian components, we used the periods P_{01}, P_{02} and epochs $T0_{01}$, $T0_{02}$ listed in ExoFOP–TESS for candidates TOI-201.01 and TOI-201.02 respectively as initial constraints. For eccentric models, we used the $(e \sin\omega, e\cos\omega)$ parameterization.

1. *no planet*. This model assumes that all the RV variations are due solely to jitter. The only free parameters are the systemic RVs and jitters for the two instruments. This model effectively provides us with a baseline log-evidence $\ln(Z) = 32.9 \pm 0.2$.
2. *one-planet, circular*. In this model, we add a Keplerian with Gaussian priors for the period and $T0$ centered on those provided by the light curve, and an eccentricity fixed to zero. We find a surprisingly low log-evidence of $\ln(Z) = 1.16 \pm 0.02$. As can be seen in Table 3, the instrumental jitter values are very similar to those of the

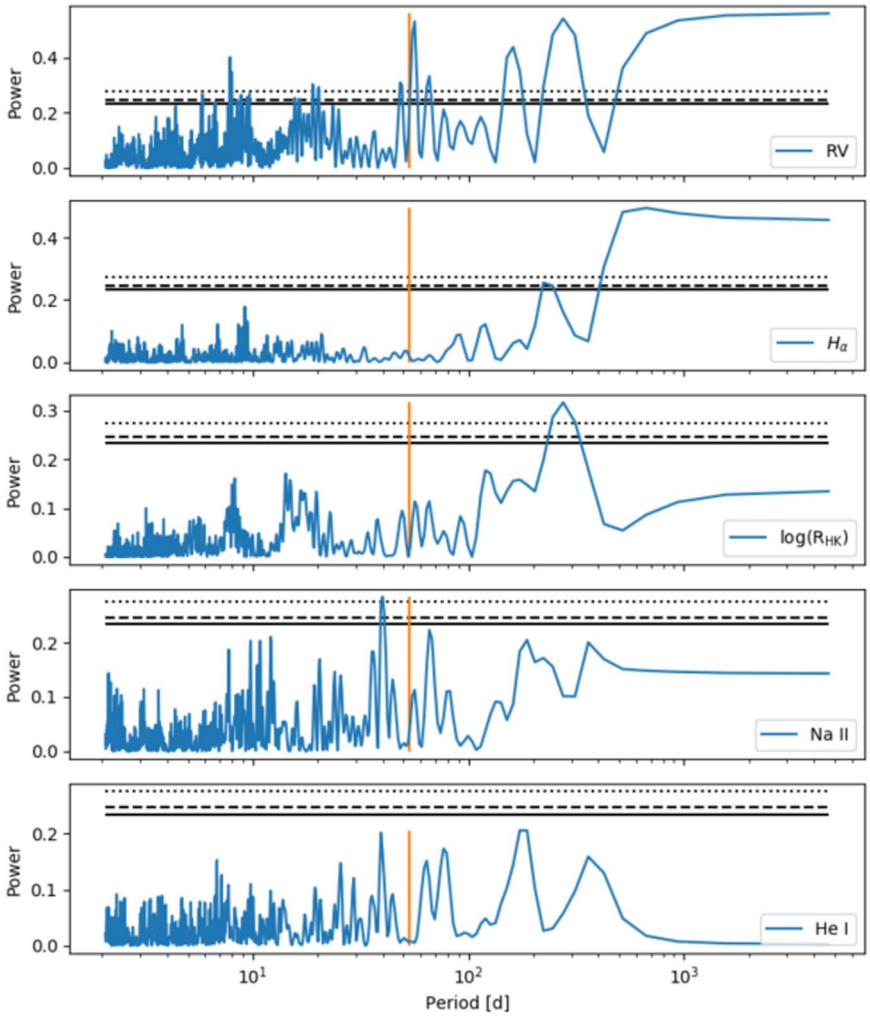

Figure 4. GLS periodograms of the joint FEROS–HARPS time series for (top to bottom) radial velocities, H_α, $\log(R'_{HK})$, Na II, and He I. The solid, dashed, and dotted horizontal black lines indicate the 1%, 0.5% and 0.01% false-alarm probability (FAP) levels respectively. The vertical orange line indicates the period of the planetary candidate TOI-201.01.

flat model, suggesting that the RV variations may be absorbed by this jitter.

3. *one-planet, eccentric*. In this model, we allow for free eccentricity and ω for the Keplerian. We find a much higher log-evidence of $\ln(Z) = 126.7 \pm 0.1$.
4. *two planets, eccentric*. In addition to the Keplerian with priors centered on the parameters of TOI-201.01, we include a second Keplerian (also with free eccentricity and ω) to represent TOI-201.02. We find a decreased log-evidence with respect to model 3 of $\ln(Z) = 25.96 \pm 0.01$, and the eccentricity for the 53 day Keplerian is increased.
5. *one-planet, eccentric, plus quadratic trend*. In this model, we test the inclusion of a quadratic trend to model long-term effects. The intercept parameter is fixed to zero, as otherwise it becomes degenerate with the instrumental offsets. We find a log-evidence of $\ln(Z) = 173.60 \pm 0.01$.
6. *one-planet, eccentric, plus GP*. In this model, we incorporate a GP, to account for stellar activity. We use an (approximate) Matern kernel, as implemented in `celerite`. We find a log-evidence of $\ln(Z) = 185.71 \pm 0.02$.

The model with a single eccentric Keplerian and a GP is clearly favored, with a $\Delta \ln Z_{6,3} \approx 59$ compared to the model with only a single eccentric planet, and better accounts for other trends in the data, with $\Delta \ln Z_{6,5} \approx 12$ compared to the model with a single eccentric planet and a quadratic trend. Likewise, the difference from the flat model is $\Delta \ln Z_{6,1} \approx 153$. This allows us to confirm the candidate planet TOI-201.01, referred to as TOI-201 b hereafter. The full model and components, and the FEROS and HARPS RVs, are shown in Figure 7.

We inspected the residuals of the RVs after subtracting model 6 to check if there were any significant periodicities remaining. In particular, we wish to verify whether there is any signal at the period of the planetary candidate TOI-201.02. Figure 8 (top panel) shows the periodogram of the residuals, with the five day period of TOI-201.02 highlighted. There is no peak at or close to this period, nor any significant signals visible. We also inspected the residuals of the RVs to model 5, to rule out the possibility that the signal could be absorbed by the GP. Figure 8 (middle panel) shows their periodogram; there are no significant signals at any period, and a peak emerges around the ~300 day period seen in the H_α and $\log(R'_{HK})$ periodograms, suggesting this model is less efficient at suppressing the long-term activity-induced RV variations.

The question arises as to whether we can expect TOI-201.02 to be detectable in RVs. We use the radius of TOI-201.02, and the revised mass–radius relations of Otegi et al. (2020), to

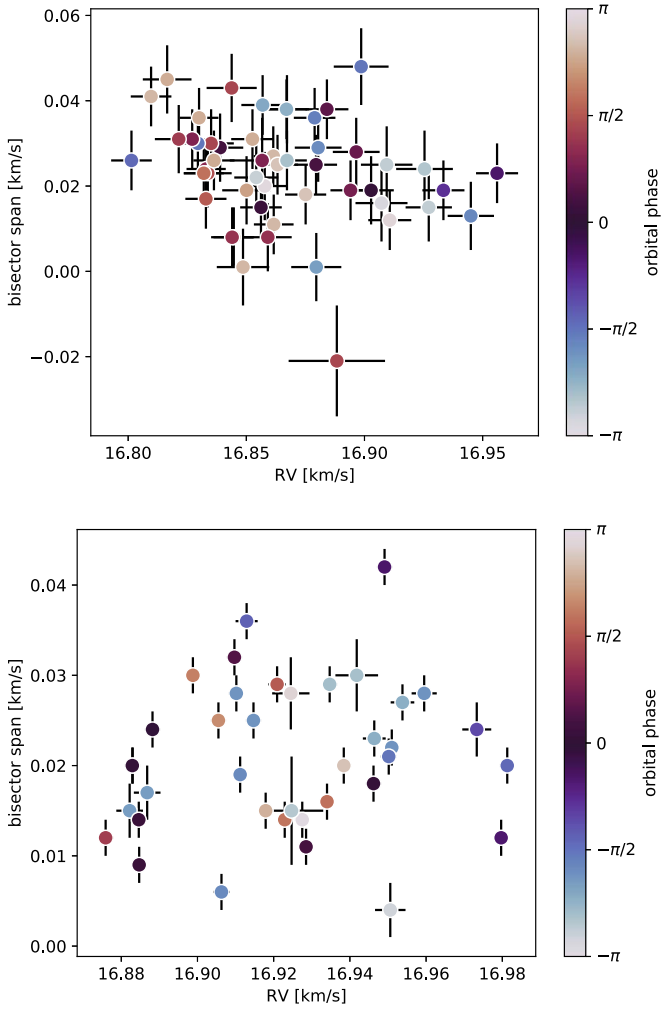

Figure 5. Bisector span as a function of radial velocity, for FEROS (top) and HARPS (bottom) data. The points are color-coded by orbital phase. No correlations are apparent.

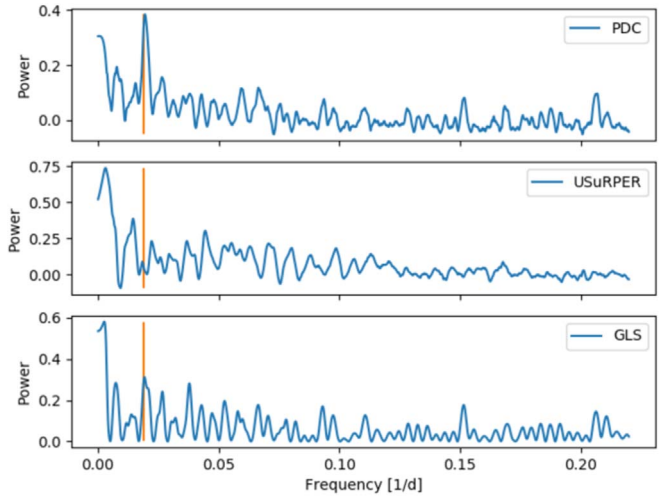

Figure 6. Phase Distance Correlation (top), USuRPER (middle), and, for comparison, GLS (bottom) periodograms of the joint FEROS–HARPS radial velocity (RV) time series. The vertical orange line indicates the period of the planetary candidate TOI-201.01. The peak at the planetary period is enhanced in the PDC periodogram compared to the GLS periodogram, and suppressed in the USuRPER periodogram which shows a peak in low frequencies.

Table 2
Prior Parameter Distributions for the Radial Velocity Analysis

Parameter	Distribution	Models
$\mu_{\rm HARPS}$ (km s^{-1})	$\mathcal{U}(-30, 30)$	1, 2, 3, 4, 5, 6
$\mu_{\rm FEROS}$ (km s^{-1})	$\mathcal{U}(-30, 30)$	1, 2, 3, 4, 5, 6
$\sigma_{\rm HARPS}$ (km s^{-1})	$\mathcal{J}(0.001, 100)$	1, 2, 3, 4, 5, 6
$\sigma_{\rm FEROS}$ (km s^{-1})	$\mathcal{J}(0.001, 100)$	1, 2, 3, 4, 5, 6
P_{01} (days)	$\mathcal{N}(52.978306, 0.1)$	2, 3, 4, 5, 6
$T0_{01}$ (days)	$\mathcal{N}(2458376.052124, 0.1)$	2, 3, 4, 5, 6
K_{01} (km s^{-1})	$\mathcal{U}(0, 1)$	2, 3, 4, 5, 6
$e \sin \omega_{01}$	$\mathcal{U}(-1, 1)$	3, 4, 5, 6
$e \cos \omega_{01}$	$\mathcal{U}(-1, 1)$	3, 4, 5, 6
P_{02} (days)	$\mathcal{N}(5.849173, 0.1)$	4
$T0_{02}$ (days)	$\mathcal{N}(2458327.244194, 0.1)$	4
K_{02} (km s^{-1})	$\mathcal{U}(0, 1)$	4
$e \sin \omega_{02}$	$\mathcal{U}(-1, 1)$	4
$e \cos \omega_{02}$	$\mathcal{U}(-1, 1)$	4
rv$_{\rm slope}$ ((km s^{-1}) day^{-1})	$\mathcal{U}(-100, 100)$	5
rv$_{\rm quad}$ ((km s^{-1}) day^{-2})	$\mathcal{U}(-100, 100)$	5
$\sigma_{\rm GP}$	$\mathcal{J}(0.01, 100)$	6
$\rho_{\rm GP}$	$\mathcal{J}(0.01, 100)$	6

Note. $\mathcal{U}(a, b)$ indicates a uniform distribution between a and b; $\mathcal{N}(a, b)$ a normal distribution with mean a and standard deviation b; $\mathcal{J}(a, b)$ a Jeffreys or log-uniform distribution between a and b.

estimate a mass of $M_p \approx 6.38\,M_\oplus$ for TOI-201.02, which leads to an RV semi-amplitude of $K \approx 1.88$ m s^{-1}. While such small amplitudes are in principle detectable with HARPS, this falls below our median RV error, and the periodogram of the residuals to model 6 for HARPS data alone (Figure 8, bottom panel) shows no significant signals. We also tested whether such a planet would be recoverable from our data by injecting a Keplerian into the randomly shuffled residuals. For the injected Keplerian, we assumed a circular orbit, and used the period and epoch from the transit data and the mass estimated from the radius. The periodogram of these RVs showed no significant signals at any period.

Although we cannot detect TOI-201.02 in the RV data, we can still use these data to estimate its maximum mass. For this, we ran a more constrained two-planet model on the FEROS and HARPS data, fixing the periods and epochs to those listed in ExoFOP–TESS. We also fixed the eccentricity of the inner planet to zero, since we can expect its orbit to be circularized by its proximity to the host star. Using the semi-amplitude of the resulting Keplerian fit, $K = 1.76^{+1.84}_{-1.14}$ m s^{-1}, we estimate a maximum mass for TOI-201.02 of $M_{\rm max} \approx 37.5\,M_\oplus$ with 98% confidence.

3.3. Joint Transit and RV Model

Having shown that TOI-201 b can be detected in the RVs alone, we perform a joint modeling of the full set of RVs and transit data. We adopt a one-planet model, with $e \sin \omega$ and $e \cos \omega$ constrained using the posteriors from model 6. We also include two separate GPs: one on the joint FEROS, HARPS, CORALIE, and MINERVA-Australis RVs, to account for the stellar activity, as done in model 6, and one on the TESS light curve, to account for instrumental effects such as the over-estimation of flux for the partial transit in Sector 8 (Figure 1, bottom panel). Rather than fit for the planet-to-star radius ratio and impact parameter of the orbit directly, we adopt the (r_1, r_2)

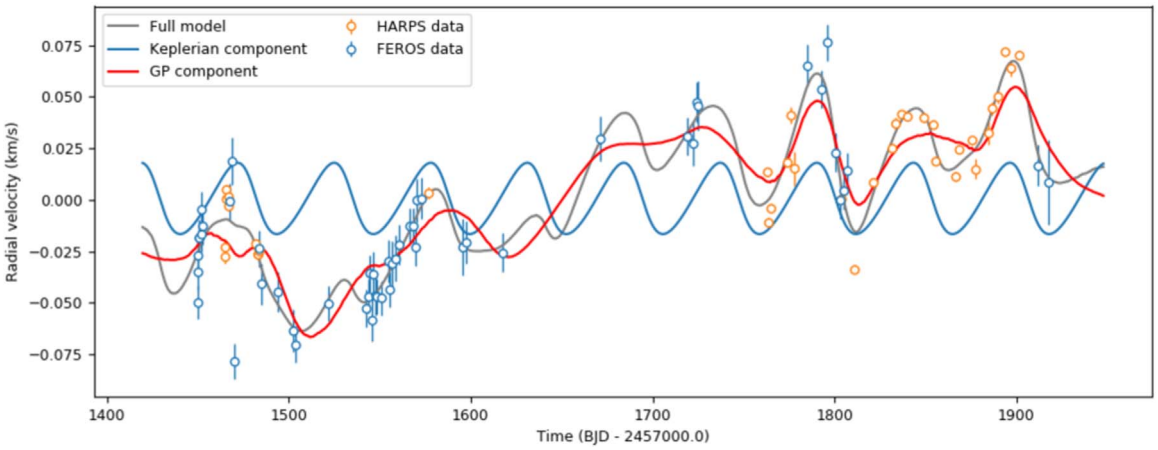

Figure 7. RV data for FEROS and HARPS, full fitted model, and Keplerian and Gaussian process (GP) model components, for the favored model of one eccentric planet plus a GP.

Table 3
Radial Velocity Analysis for the Different Models Tested

Parameter	Flat Model (1)	1 Planet Circ. (2)	1 Planet Ecc. (3)	2 Planet Ecc. (4)	1 Planet + quad (5)	1 Planet + GP (6)
$\mu_{\rm HARPS}$ (km s^{-1})	$16.999^{+0.009}_{-0.038}$	$16.92^{+0.01}_{-0.01}$	$16.92^{+0.01}_{-0.01}$	$17.04^{+0.04}_{-0.05}$	$16.884^{+0.003}_{-0.004}$	$16.91^{+0.05}_{-0.06}$
$\mu_{\rm FEROS}$ (km s^{-1})	$16.983^{+0.010}_{-0.002}$	$16.834^{+0.004}_{-0.003}$	$16.875^{+0.005}_{-0.006}$	$16.89^{+0.01}_{-0.01}$	$16.855^{+0.003}_{-0.004}$	$16.88^{+0.05}_{-0.06}$
$\sigma_{\rm HARPS}$ (km s^{-1})	$0.148^{+0.007}_{-0.009}$	$0.157^{+0.003}_{-0.003}$	$0.068^{+0.012}_{-0.008}$	$0.40^{+0.05}_{-0.04}$	$0.011^{+0.002}_{-0.001}$	$0.012^{0.001}_{0.001}$
$\sigma_{\rm FEROS}$ (km s^{-1})	$0.189^{+0.013}_{-0.005}$	$0.294^{+0.006}_{-0.004}$	$0.047^{+0.005}_{-0.006}$	$0.093^{+0.010}_{-0.008}$	$0.020^{+0.003}_{-0.002}$	$0.013^{0.002}_{0.002}$
P_{01} (days)	...	$52.787^{+0.006}_{-0.006}$	$52.99^{+0.08}_{-0.09}$	$53.03^{+0.04}_{-0.06}$	$53.04^{+0.08}_{-0.09}$	$53.04^{+0.05}_{-0.06}$
$T0_{01}$ (days)	...	$2458376.130^{+0.07}_{-0.009}$	$2458375.97^{+0.04}_{-0.05}$	$2458376.00^{+0.05}_{-0.04}$	$2458376.1^{+0.1}_{-0.1}$	$2458376.11^{+0.05}_{-0.05}$
K_{01} (km s^{-1})	...	$0.054^{+0.005}_{-0.005}$	$0.027^{+0.014}_{-0.009}$	$0.08^{+0.04}_{-0.04}$	$0.026^{+0.003}_{-0.003}$	$0.016^{+0.005}_{-0.005}$
$e \sin \omega_{01}$	...	...	$0.44^{+0.19}_{-0.22}$	$0.30^{+0.25}_{-0.33}$	$0.31^{+0.09}_{-0.09}$	$0.20^{+0.16}_{-0.19}$
$e \cos \omega_{01}$	...	...	$0.21^{+0.16}_{-0.12}$	$0.50^{+0.18}_{-0.36}$	$0.03^{+0.09}_{-0.08}$	$-0.10^{+0.19}_{-0.20}$
e_{01}	...	...	$0.52^{+0.18}_{-0.20}$	$0.64^{+0.18}_{-0.29}$	$0.32^{+0.09}_{-0.09}$	$0.30^{+0.16}_{-0.13}$
ω_{01} (deg)	...	...	61^{+18}_{-18}	33^{+26}_{-17}	85^{+16}_{-14}	110^{+39}_{-45}
P_{02} (days)	...	...	...	$5.85^{+0.03}_{-0.05}$	...	...
$T0_{02}$ (days)	...	...	...	$2458327.16^{+0.04}_{-0.05}$	...	...
K_{02} (m s^{-1})	...	...	...	$0.02^{+0.02}_{-0.01}$	...	...
$e \sin \omega_{02}$	...	...	...	$-0.08^{+0.28}_{-0.19}$	...	...
$\cos \omega_{02}$	...	...	...	$-0.56^{+0.41}_{-0.28}$	...	...
e_{02}	...	...	...	$0.62^{+0.27}_{-0.34}$	...	...
ω_{02}	...	...	...	156^{+18}_{-35}	...	...
$\mathrm{rv}_{\rm slope}$ ((km s^{-1}) day^{-1})	...	...	...	...	$0.00009^{+0.00005}_{-0.00005}$	...
$\mathrm{rv}_{\rm quad}$ ((km s^{-1}) day^{-2})	...	...	...	...	$0.00000013^{+0.00000011}_{-0.00000011}$	...
$\sigma_{\rm GP}$	...	...	...	...	...	$0.10^{+0.04}_{-0.02}$
$\rho_{\rm GP}$	...	...	...	...	...	55^{+20}_{-14}
$\ln(Z)$	32.9 ± 0.2	1.16 ± 0.02	126.7 ± 0.1	25.96 ± 0.01	173.60 ± 0.01	185.71 ± 0.02
$\Delta \ln Z_{\rm i}$	...	≈ -32	≈ 94	≈ -7	≈ 141	≈ 153

Note. Top: posterior parameter distributions. Bottom: log-evidence and difference to the baseline no-planet model. Model 6 is the final adopted model.

parameterization of Espinoza (2018), which allows for efficient sampling with uniform priors.

We find a log-evidence of $\ln(Z) = 1236042.914 \pm 0.008$. The priors are listed in Table 4, and the posteriors in Table 5. Figure 9 shows the phase-folded data and the full model for the light curves and RVs. Using the stellar parameters obtained in Section 3.1, and the posterior distributions of the full model, we compute a mass of $0.42^{+0.05}_{-0.03}\ M_{\rm J}$ and a radius of $1.008^{+0.012}_{-0.015}\ R_{\rm J}$ for TOI-201 b. The physical parameters and derived orbital parameters are also listed in Table 5.

The MINERVA-Australis RVs have larger error bars and show more dispersion from the fitted model than those of the other three RV data sets, as can be clearly seen in Figure 9((b), bottom panel). Therefore, we also tested an analogous model in which the MINERVA-Australis RVs were not included. The resulting parameters are the same within uncertainties, and the uncertainties on the parameters are similar for both models. This being the case, we prefer the model including the MINERVA-Australis RVs.

4. Discussion and Conclusions

We have presented confirmation through RVs of the transiting planet TOI-201 b. In addition to the RV signal due to TOI-201 b, we also see long-period signals in both the RVs

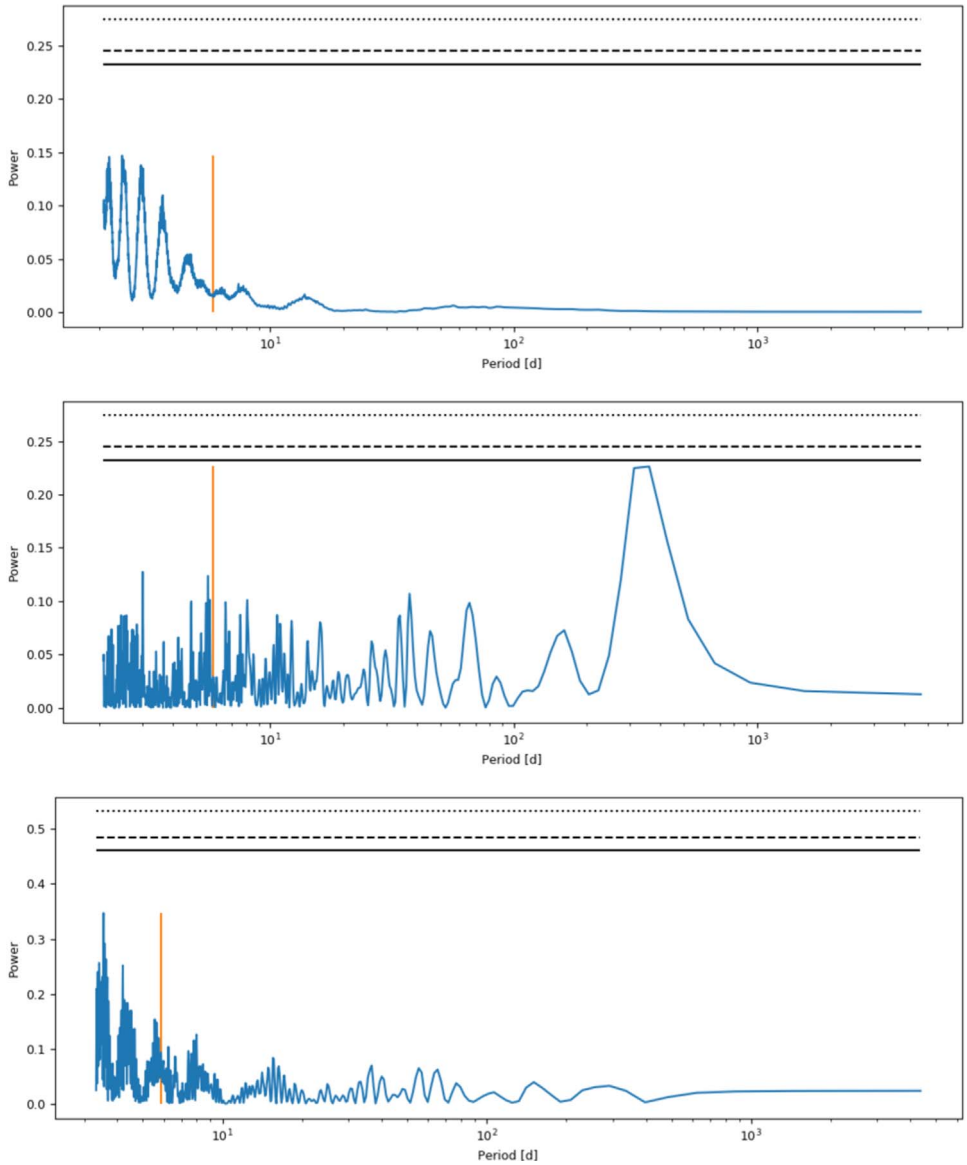

Figure 8. Periodogram of the RV residuals to models 6 (top) and 5 (middle) for the full RV data set, and of the RV residuals to model 6 for the HARPS data alone (bottom). The vertical line indicates the period of the planetary candidate TOI-201.02. There are no significant signals in any of the periodograms.

and in the H_α and $\log(R'_{HK})$ activity indicators. We therefore conclude that the long-period variations in RV are likely due to stellar activity, and model them using a GP.

We were unable to confirm the second planetary candidate around this star, TOI-201.02. Two-planet fits to the RVs are not favored by likelihood comparison, and there are no signals at ~5.8 days in the RV residuals to the one-planet fit. Likewise, we were not able to retrieve a Keplerian, modeled using the candidate's period and estimated mass, that we injected into the randomly shuffled residuals of the one-planet model.

TOI-201 b is an eccentric warm giant, orbiting a young F-type star. More specifically, TOI-201 falls within the youngest 5% of exoplanet host stars with measured ages,[35] making this system a valuable addition to the known planets around young stars, which are important for testing and constraining planet formation and evolution theories (e.g., Baraffe et al. 2008; Mordasini et al. 2012a, 2012b). At $\lesssim$ 1 Gyr, some evolutionary processes that are typically not observable are still ongoing, such as photoevaporation of planetary envelopes (David et al. 2011) for small planets. Likewise, giant planet formation theory has difficulties fixing the luminosity of a cooling planet as a function of time ("hot start" versus "cool start" models; e.g., Mordasini et al. 2012b), and representatives of giant planets that are currently cooling may help to constrain that. TOI-201 b also joins the small but growing population of longer-period giant planets, helping to populate a still relatively sparse region of the radius–period diagram (Figure 10). On this diagram, it is located closest to Kepler-117 c (period 50.790391 ± 0.000014 days, radius $1.101 \pm 0.035\,R_J$, mass $1.84 \pm 0.18\,M_J$, eccentricity 0.0323 ± 0.0033; Bruno et al. 2015) and Kepler-30 c (period 60.32503 ± 0.00010 days, radius $1.069 \pm 0.025\,R_J$, mass $1.686 \pm 0.016\,M_J$, eccentricity 0.0115 ± 0.0005; Panichi et al. 2018) but is noticeably less massive and dense, and more eccentric, than both these planets. Given the relative youth of the TOI-201 system, with a stellar

[35] According to the ages reported in the NASA Exoplanet Archive, located at https://exoplanetarchive.ipac.caltech.edu/index.html.

Table 4
Prior Parameter Distributions for the Joint Transit and Radial Velocity Analysis

Parameter	Distribution
$\mu_{\rm HARPS}$ (km s^{-1})	$\mathcal{U}(16.85, 16.96)$
$\mu_{\rm FEROS}$ (km s^{-1})	$\mathcal{U}(16.82, 16.93)$
$\mu_{\rm CORALIE}$ (km s^{-1})	$\mathcal{U}(-30, 30)$
$\mu_{\rm MINERVA}$ (km s^{-1})	$\mathcal{U}(-30, 30)$
$\sigma_{\rm HARPS}$ (km s^{-1})	$\mathcal{J}(0.011, 0.013)$
$\sigma_{\rm FEROS}$ (km s^{-1})	$\mathcal{J}(0.011, 0.015)$
$\sigma_{\rm CORALIE}$ (km s^{-1})	$\mathcal{J}(0.001, 100)$
$\sigma_{\rm MINERVA}$ (km s^{-1})	$\mathcal{J}(0.001, 100)$
P_b (days)	$\mathcal{N}(52.978306, 0.1)$
$T0_b$ (days)	$\mathcal{N}(2458376.052124, 0.1)$
K_b (km s^{-1})	$\mathcal{U}(0.011, 0.021)$
$e \sin \omega_{\rm b}$	$\mathcal{U}(0.01, 0.36)$
$e \cos \omega_{\rm b}$	$\mathcal{U}(-0.30, 0.09)$
$\sigma_{\rm GP,RV}$	$\mathcal{J}(0.01, 100)$
$\rho_{\rm GP,RV}$	$\mathcal{J}(0.01, 100)$
$r_{1,\rm b}$	$\mathcal{U}(0, 1)$
$r_{2,b}$	$\mathcal{U}(0, 1)$
ρ	$\mathcal{J}(100., 10000.)$
$q_{1,\rm TESS}$	$\mathcal{U}(0, 1)$
$q_{2,\rm TESS}$	$\mathcal{U}(0, 1)$
$m_{\rm d,TESS}$	1.0 (fixed)
$m_{\rm flux,TESS}$	$\mathcal{N}(0, 0.1)$
$\sigma_{\rm TESS}$	$\mathcal{J}(0.1, 1000)$
$\sigma_{\rm GP,TESS}$	$\mathcal{J}(1 \times 10^{-6}, 1000000)$
$\rho_{\rm GP,TESS}$	$\mathcal{J}(0.001, 1000)$
$q_{1,\rm NGTS}$	$\mathcal{U}(0, 1)$
$q_{2,\rm NGTS}$	$\mathcal{U}(0, 1)$
$m_{\rm d,NGTS}$	1.0 (fixed)
$m_{\rm flux,NGTS}$	$\mathcal{N}(0, 0.1)$
$\sigma_{\rm NGTS}$	$\mathcal{J}(0.1, 1000)$

Note. $\mathcal{U}(a, b)$ indicates a uniform distribution between a and b; $\mathcal{N}(a, b)$ a normal distribution with mean a and standard deviation b; $\mathcal{J}(a, b)$ a Jeffreys or log-uniform distribution between a and b.

Table 5
Parameters for Planet TOI-201 b

Parameter	Distribution
$\mu_{\rm HARPS}$ (km s^{-1})	$16.92^{+0.01}_{-0.01}$
$\mu_{\rm FEROS}$ (km s^{-1})	$16.89^{+0.01}_{-0.01}$
$\mu_{\rm CORALIE}$ (km s^{-1})	$16.87^{+0.02}_{-0.01}$
$\mu_{\rm MINERVA}$ (km s^{-1})	$0.02^{+0.01}_{-0.01}$
$\sigma_{\rm HARPS}$ (km s^{-1})	$0.0117^{+0.0008}_{-0.0005}$
$\sigma_{\rm FEROS}$ (km s^{-1})	$0.014^{+0.001}_{-0.001}$
$\sigma_{\rm CORALIE}$ (km s^{-1})	$0.019^{+0.009}_{-0.007}$
$\sigma_{\rm MINERVA}$ (km s^{-1})	$0.026^{+0.004}_{-0.004}$
P_b (days)	$52.97818^{+0.00004}_{-0.00004}$
$T0_b$ (BJD)	$2458376.0520^{+0.0003}_{-0.0003}$
K_b (km s^{-1})	$0.019^{+0.001}_{-0.002}$
$e \sin \omega_{\rm b}$	$0.28^{+0.06}_{-0.09}$
$e \cos \omega_{\rm b}$	$0.04^{+0.04}_{-0.07}$
$\sigma_{\rm GP}$	$0.025^{+0.008}_{-0.006}$
$\rho_{\rm GP}$	70^{+21}_{-27}
$r_{1,\rm b}$	$0.82^{+0.01}_{-0.01}$
$r_{2,\rm b}$	$0.0786^{+0.0010}_{-0.0007}$
ρ	854^{+288}_{-154}
$q_{1,\rm TESS}$	$0.22^{+0.06}_{-0.06}$
$q_{2,\rm TESS}$	$0.25^{+0.33}_{-0.18}$
$m_{\rm d,TESS}$	1.0
$m_{\rm flux,TESS}$	$-0.00002^{+0.00002}_{-0.00002}$
$\sigma_{\rm TESS}$	73^{+5}_{-5}
$\sigma_{\rm GP,TESS}$	$0.00030^{+0.00001}_{-0.00001}$
$\rho_{\rm GP,TESS}$	$0.64^{+0.03}_{-0.03}$
$q_{1,\rm NGTS}$	$0.47^{+0.23}_{-0.19}$
$q_{2,\rm NGTS}$	$0.38^{+0.32}_{-0.25}$
$m_{\rm d,NGTS}$	1.0
$m_{\rm flux,NGTS}$	$0.0001^{+0.0002}_{-0.0002}$
$\sigma_{\rm NGTS}$	5^{+56}_{-4}
e_b	$0.28^{+0.06}_{-0.09}$
$\omega_{\rm b}$ [deg]	82^{+14}_{-9}
a [au]	$0.30^{+0.02}_{-0.03}$
M_b [$M_{\rm J}$]	$0.42^{+0.05}_{-0.03}$
R_b [$R_{\rm J}$]	$1.008^{+0.012}_{-0.015}$
$T_{\rm eq}$ [a] [K]	759^{+37}_{-26}

Notes. Top: posterior parameter distributions for the joint transit and RV Analysis. Bottom: derived orbital parameters and physical parameters.
[a] Time-averaged equilibrium temperature, using Equation (16) of Méndez & Rivera-Valentín (2017) assuming bond albedo $A = 0$, heat distribution $\beta = 0.5$, and emissivity $\epsilon = 1$.

age of $0.87^{+0.46}_{-0.49}$ Gyr (for comparison, Bruno et al. 2015 find an age of 5.3 ± 1.4 Gyr for Kepler-117), the difference in density may be partly explained by a still-contracting TOI-201 b.

As noted in the introduction, the size and mass of warm Jupiters is determined by their metallicity. We use the structure models of Thorngren & Fortney (2019) to constrain the heavy element mass for TOI-201 b. Using the planet mass and insolation flux, and the stellar age, we employ a retrieval algorithm to recover the metallicity that would match the observed radius. The metallicity required to explain the planet's radius is strongly correlated with the age, indicating that it appears to still be cooling—and therefore contracting—fairly rapidly. The bulk metallicity we obtain is $Z_p = 0.16^{+0.03}_{-0.02}$, which is moderately low for the planet's mass compared to similarly massive planets from Thorngren & Fortney (2019), but still within the range of values obtained in that work. Given the high precision on the planetary parameters, modeling uncertainty (e.g., in the equation of state) is probably larger than the statistical uncertainty from the parameters. We estimate this at around a 20% relative uncertainty, though recent work by Müller et al. (2020) cautions that the interplay between various model assumptions (particularly in the choice of equations of state, the distribution of heavy elements, and the modeling of its effect on the opacity) may mean it is higher.

The posterior distribution of the parameters is shown in Figure 11.

The Rossiter–McLaughlin effect (McLaughlin 1924; Rossiter 1924) allows the stellar obliquity to be measured. These measurements are useful for constraining migration scenarios, and are particularly valuable for planets such as TOI-201 b, which are located at longer orbital distances where tidal realignment is no longer in play (see, e.g., Triaud 2018 for a review). It is worth noting that all the RV measurements used in the analysis in Section 3 fall outside the transit, and so are not affected by the Rossiter–McLaughlin effect. For TOI-201 b, the expected semi-amplitude of the Rossiter–McLaughlin signal is $\approx$40 m s^{-1} for an aligned orbit (using the equation of Winn 2010), making this system a good candidate for such observations.

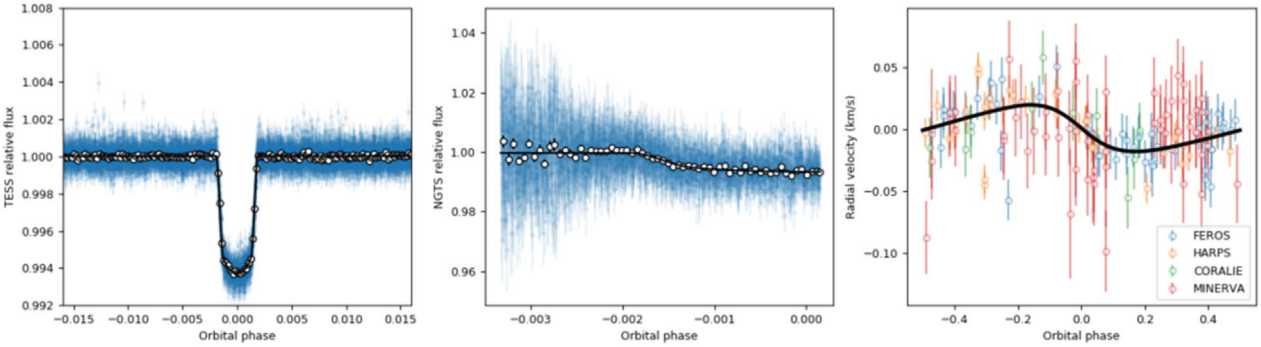

(a)

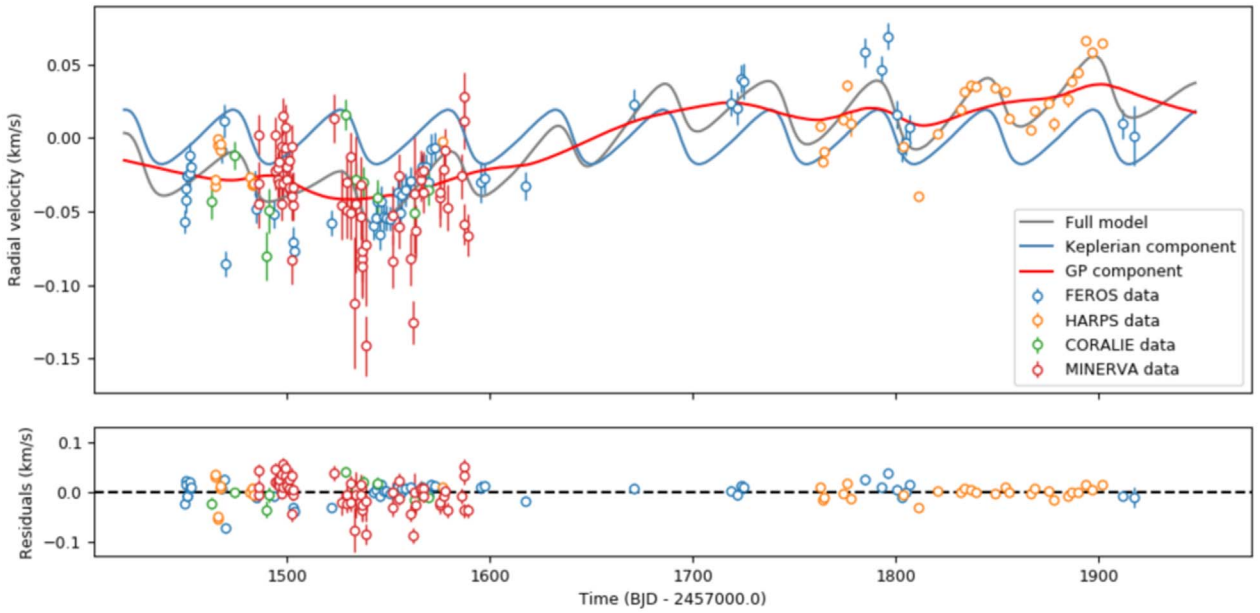

(b)

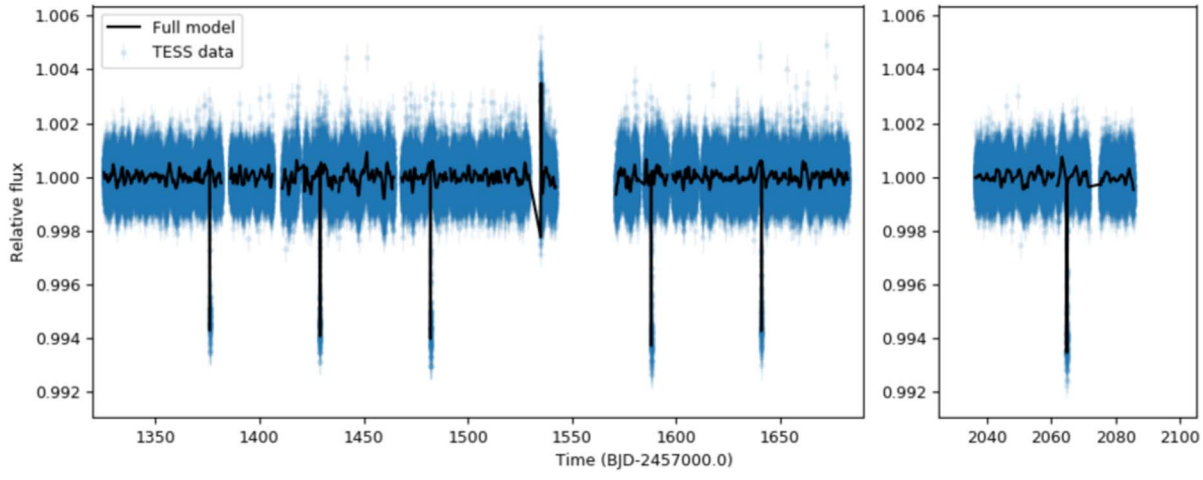

(c)

Figure 9. Joint transit and RV model. (a) Left panel: phase-folded TESS data (blue points), binned TESS data (white points) and model (black line). Center panel: as left, for Next Generation Transit Survey data. Right panel: phase-folded FEROS, HARPS, CORALIE, and MINERVA-Australis radial velocities, with the RV GP component removed, and Keplerian model component (black line). (b) Top: RV data for FEROS, HARPS, CORALIE, and MINERVA-Australis, full model, and Keplerian and GP components. Bottom: RV residuals. (c) TESS data and full model for Sectors 1–13 (left panel) and 27–28 (right panel).

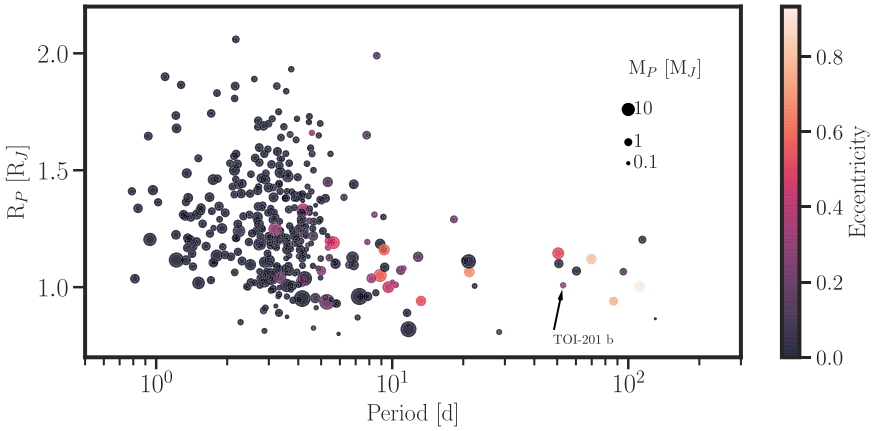

Figure 10. Radius–period diagram for giant planets ($R_p \geqslant 0.8\,R_J$), with masses and radii measured to better than 25%, obtained from the TEPCAT catalog (Southworth 2011). The markers are scaled by planet mass and color-coded by eccentricity. TOI-201 b is labeled.

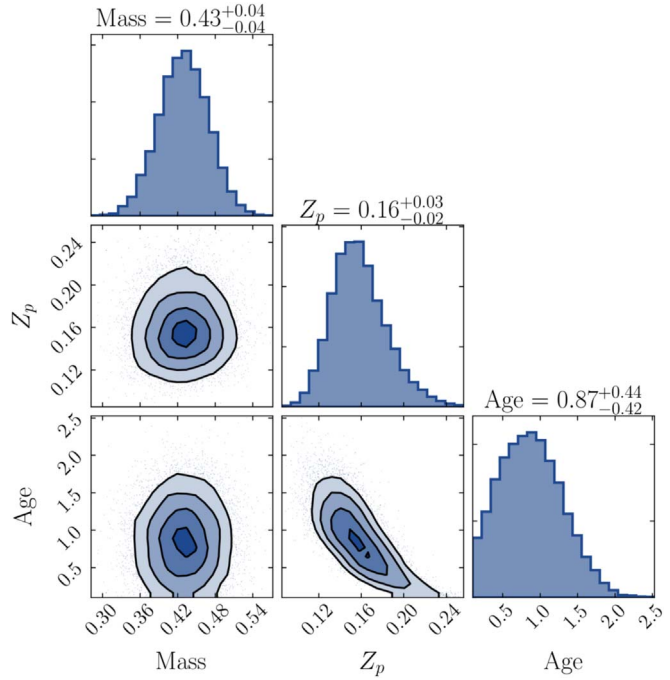

Figure 11. Posterior distribution of heavy elements, age, and mass, from the structure models of Thorngren & Fortney (2019).

This paper includes data collected by the TESS mission, which are publicly available from the Mikulski Archive for Space Telescopes (MAST). Funding for the TESS mission is provided by NASA's Science Mission directorate.

This research has made use of the Exoplanet Follow-up Observation Program website, which is operated by the California Institute of Technology, under contract with the National Aeronautics and Space Administration under the Exoplanet Exploration Program. We acknowledge the use of public TESS Alert data from the pipelines at the TESS Science Office and at the TESS Science Processing Operations Center.

Resources supporting this work were provided by the NASA High-End Computing (HEC) Program through the NASA Advanced Supercomputing (NAS) Division at Ames Research Center for the production of the SPOC data products.

M.H., A.J. and R.B. acknowledge support from ANID—Millennium Science Initiative—ICN12_009. A.J. acknowledges additional support from FONDECYT project 1171208. T.H. acknowledges support from the European Research Council under the Horizon 2020 Framework Program via the ERC Advanced Grant Origins 83 24 28. T.D. acknowledges support from MIT's Kavli Institute as a Kavli postdoctoral fellow. S.Z. acknowledges support by the ISRAEL SCIENCE FOUNDATION (grant No. 848/16) and also partial support by the Ministry of Science, Technology and Space, Israel.

We thank the Swiss National Science Foundation (SNSF) and the Geneva University for their continuous support to our planet search programmes. This work has been in particular carried out in the frame of the National Centre for Competence in Research "PlanetS" supported by the Swiss National Science Foundation (SNSF).

MINERVA-Australis is supported by Australian Research Council LIEF Grant LE160100001, Discovery Grant DP180100972, Mount Cuba Astronomical Foundation, and institutional partners University of Southern Queensland, UNSW Sydney, MIT, Nanjing University, George Mason University, University of Louisville, University of California Riverside, University of Florida, and The University of Texas at Austin. We respectfully acknowledge the traditional custodians of all lands throughout Australia, and recognize their continued cultural and spiritual connection to the land, waterways, cosmos, and community. We pay our deepest respects to all Elders, ancestors and descendants of the Giabal, Jarowair, and Kambuwal nations, upon whose lands the MINERVA-Australis facility at Mt Kent is situated.

Facilities: TESS, FEROS/MPG2.2 m, HARPS/ESO3.6 m, CORALIE, MINERVA-Australis, NGTS, HRCam/SOAR.

Software: CERES (Brahm et al. 2017a), juliet (Espinoza et al. 2019), ZASPE (Brahm et al. 2017b), radvel (Fulton et al. 2018), emcee (Foreman-Mackey et al. 2013), MultiNest (Feroz et al. 2009), PyMultiNest (Buchner et al. 2014), batman (Kreidberg 2015), celerite (Foreman-Mackey et al. 2017).

Appendix
RV and Activity Indices

In this Appendix, we present the RVs and activity indices, where applicable. Table A1 shows the data for FEROS, and Table A2 the data for HARPS, both computed using the CERES pipeline. Table A3 shows the RVs obtained from the CORALIE spectra. Table A4 shows the RVs obtained from the MINERVA-Australis spectra.

Table A1
Radial Velocity and Activity Indices Obtained from the FEROS Spectra

BJD–2457000 (days)	RV (km s^{-1})	Bisector	FWHM	S/N	H_α	$\log(R'_{HK})$	Na II	He I
2458449.72902056	16.8300 ± 0.0082	0.036 ± 0.007	15.5668	193	0.1075 ± 0.0009	−4.749 ± 0.026	0.3978 ± 0.0020	0.4992 ± 0.0025
2458449.82501961	16.8526 ± 0.0090	0.031 ± 0.007	15.6119	168	0.1076 ± 0.0010	−4.726 ± 0.026	0.3912 ± 0.0022	0.5022 ± 0.0028
2458449.81907519	16.8447 ± 0.0086	0.008 ± 0.007	15.6457	182	0.1065 ± 0.0009	−4.741 ± 0.027	0.3910 ± 0.0021	0.5019 ± 0.0026
2458450.78211913	16.8616 ± 0.0084	0.011 ± 0.007	15.6056	187	0.1070 ± 0.0009	−4.757 ± 0.027	0.3982 ± 0.0020	0.5033 ± 0.0026
2458450.77751112	16.8614 ± 0.0083	0.027 ± 0.007	15.6184	191	0.1064 ± 0.0009	−4.739 ± 0.026	0.3979 ± 0.0020	0.5012 ± 0.0026
2458451.80088761	16.8751 ± 0.0087	0.018 ± 0.007	15.6244	179	0.1087 ± 0.0010	−4.705 ± 0.025	0.3923 ± 0.0021	0.5011 ± 0.0027
2458451.80550488	16.8632 ± 0.0087	0.025 ± 0.007	15.6687	177	0.1090 ± 0.0010	−4.756 ± 0.027	0.3908 ± 0.0021	0.4983 ± 0.0027
2458452.81008207	16.8672 ± 0.0093	0.038 ± 0.008	15.6380	161	0.1093 ± 0.0011	−4.714 ± 0.026	0.4017 ± 0.0024	0.4986 ± 0.0030
2458467.81642493	16.8789 ± 0.0088	0.036 ± 0.007	15.5752	174	0.1081 ± 0.0010	−4.715 ± 0.026	0.3830 ± 0.0022	0.4967 ± 0.0026
2458468.80955367	16.8986 ± 0.0116	0.048 ± 0.009	15.6108	115	0.1101 ± 0.0016	−4.771 ± 0.033	0.3838 ± 0.0035	0.5044 ± 0.0041
2458469.81379926	16.8014 ± 0.0086	0.026 ± 0.007	15.7449	184	0.1051 ± 0.0010	−4.764 ± 0.028	0.3908 ± 0.0021	0.5026 ± 0.0026
2458483.80487685	16.8562 ± 0.0088	0.015 ± 0.007	15.6195	174	0.1103 ± 0.0010	−4.734 ± 0.027	0.3971 ± 0.0022	0.5024 ± 0.0028
2458484.68236998	16.8389 ± 0.0098	0.029 ± 0.008	15.6311	147	0.1139 ± 0.0012	−4.728 ± 0.028	0.3916 ± 0.0025	0.4989 ± 0.0032
2458493.74536456	16.8351 ± 0.0096	0.030 ± 0.008	15.6102	152	0.1136 ± 0.0012	−4.770 ± 0.030	0.3987 ± 0.0025	0.4949 ± 0.0032
2458502.71190832	16.8165 ± 0.0103	0.045 ± 0.008	15.6693	136	0.1140 ± 0.0014	−4.760 ± 0.029	0.3852 ± 0.0029	0.4974 ± 0.0035
2458503.66565834	16.8097 ± 0.0086	0.041 ± 0.007	15.6483	179	0.1081 ± 0.0010	−4.775 ± 0.028	0.3916 ± 0.0021	0.4952 ± 0.0025
2458521.58681966	16.8295 ± 0.0087	0.030 ± 0.007	15.5953	176	0.1123 ± 0.0010	−4.737 ± 0.026	0.3975 ± 0.0021	0.4946 ± 0.0027
2458542.59373287	16.8271 ± 0.0090	0.031 ± 0.007	15.6742	170	0.1095 ± 0.0010	−4.762 ± 0.028	0.3817 ± 0.0022	0.4945 ± 0.0027
2458543.57904173	16.8330 ± 0.0083	0.024 ± 0.007	15.6701	191	0.1076 ± 0.0009	−4.760 ± 0.027	0.3774 ± 0.0020	0.4961 ± 0.0024
2458544.66708564	16.8440 ± 0.0089	0.008 ± 0.007	15.7129	171	0.1067 ± 0.0010	−4.804 ± 0.034	0.3864 ± 0.0022	0.4961 ± 0.0028
2458545.62781982	16.8214 ± 0.0101	0.031 ± 0.008	15.6486	141	0.1071 ± 0.0013	−4.792 ± 0.033	0.3856 ± 0.0028	0.4884 ± 0.0035
2458546.64551855	16.8438 ± 0.0106	0.043 ± 0.008	15.7462	132	0.1109 ± 0.0014	−4.804 ± 0.036	0.3896 ± 0.0029	0.4950 ± 0.0036
2458547.57166286	16.8337 ± 0.0101	0.023 ± 0.008	15.6793	141	0.1092 ± 0.0013	−4.794 ± 0.032	0.3938 ± 0.0028	0.4926 ± 0.0034
2458548.62966483	16.8329 ± 0.0087	0.017 ± 0.007	15.7019	179	0.1068 ± 0.0010	−4.777 ± 0.029	0.3909 ± 0.0022	0.4973 ± 0.0028
2458550.64407369	16.8320 ± 0.0085	0.023 ± 0.007	15.6949	184	0.1087 ± 0.0010	−4.816 ± 0.033	0.3901 ± 0.0021	0.4930 ± 0.0027
2458554.63465672	16.8501 ± 0.0103	0.019 ± 0.008	15.7519	138	0.1140 ± 0.0014	−4.781 ± 0.033	0.4019 ± 0.0028	0.4969 ± 0.0035
2458555.62085265	16.8363 ± 0.0087	0.026 ± 0.007	15.7304	177	0.1089 ± 0.0010	−4.767 ± 0.029	0.4028 ± 0.0022	0.4978 ± 0.0027
2458556.65947799	16.8486 ± 0.0111	0.001 ± 0.009	15.7611	124	0.1107 ± 0.0015	−4.797 ± 0.041	0.4070 ± 0.0032	0.4969 ± 0.0037
2458558.59692547	16.8513 ± 0.0113	0.035 ± 0.009	15.7526	121	0.1134 ± 0.0016	−4.791 ± 0.034	0.4061 ± 0.0032	0.4972 ± 0.0038
2458560.65048512	16.8578 ± 0.0097	0.020 ± 0.008	15.8235	152	0.1092 ± 0.0013	−4.782 ± 0.036	0.3930 ± 0.0027	0.4934 ± 0.0031
2458566.60098112	16.8672 ± 0.0084	0.026 ± 0.007	15.7052	187	0.1078 ± 0.0009	−4.763 ± 0.030	0.3895 ± 0.0021	0.4959 ± 0.0025
2458568.56334852	16.8670 ± 0.0087	0.038 ± 0.007	15.6716	177	0.1098 ± 0.0010	−4.749 ± 0.028	0.3948 ± 0.0022	0.4946 ± 0.0026
2458569.55147254	16.8569 ± 0.0090	0.039 ± 0.007	15.6554	168	0.1100 ± 0.0011	−4.780 ± 0.030	0.3890 ± 0.0023	0.4970 ± 0.0028
2458570.59258685	16.8796 ± 0.0106	0.001 ± 0.008	15.6557	132	0.1094 ± 0.0014	−4.789 ± 0.035	0.3898 ± 0.0030	0.4984 ± 0.0035
2458572.59221071	16.8804 ± 0.0099	0.029 ± 0.008	15.7094	146	0.1083 ± 0.0013	−4.746 ± 0.031	0.3868 ± 0.0027	0.5050 ± 0.0034
2458595.50775173	16.8567 ± 0.0137	0.026 ± 0.010	15.5962	93	0.1176 ± 0.0020	−4.822 ± 0.046	0.3869 ± 0.0043	0.4957 ± 0.0052
2458597.49996378	16.8591 ± 0.0101	0.008 ± 0.008	15.6091	143	0.1135 ± 0.0013	−4.762 ± 0.031	0.3817 ± 0.0027	0.4962 ± 0.0033
2458617.50211498	16.8542 ± 0.0093	0.022 ± 0.008	15.7453	161	0.1088 ± 0.0011	−4.790 ± 0.044	0.4038 ± 0.0024	0.4957 ± 0.0030
2458670.93647358	16.9094 ± 0.0109	0.025 ± 0.009	15.6949	126	0.1051 ± 0.0014	−4.739 ± 0.054	0.3878 ± 0.0030	0.4915 ± 0.0036
2458718.87031042	16.9107 ± 0.0091	0.012 ± 0.007	15.6143	165	0.1108 ± 0.0011	−4.748 ± 0.028	0.3934 ± 0.0024	0.4885 ± 0.0029
2458721.92050686	16.9072 ± 0.0110	0.016 ± 0.009	15.6205	124	0.1099 ± 0.0014	−4.706 ± 0.028	0.3911 ± 0.0032	0.4924 ± 0.0038
2458723.89624752	16.9272 ± 0.0098	0.015 ± 0.008	15.6508	147	0.1089 ± 0.0012	−4.748 ± 0.029	0.3958 ± 0.0026	0.4913 ± 0.0032
2458724.92469963	16.9254 ± 0.0120	0.024 ± 0.009	15.6280	111	0.1102 ± 0.0016	−4.724 ± 0.031	0.3926 ± 0.0035	0.4925 ± 0.0043
2458784.85036502	16.9450 ± 0.0098	0.013 ± 0.008	15.5626	147	0.1071 ± 0.0012	−4.783 ± 0.030	0.3894 ± 0.0026	0.4911 ± 0.0032
2458792.78919017	16.9334 ± 0.0089	0.019 ± 0.007	15.6070	171	0.1054 ± 0.0010	−4.770 ± 0.028	0.3861 ± 0.0023	0.4970 ± 0.0028
2458795.78669357	16.9561 ± 0.0089	0.023 ± 0.007	15.5507	170	0.1059 ± 0.0010	−4.762 ± 0.028	0.3883 ± 0.0023	0.4904 ± 0.0027
2458800.72101439	16.9028 ± 0.0096	0.019 ± 0.008	15.5996	150	0.1079 ± 0.0012	−4.789 ± 0.031	0.3859 ± 0.0026	0.4981 ± 0.0031
2458802.84973114	16.8795 ± 0.0089	0.025 ± 0.007	15.5810	171	0.1075 ± 0.0010	−4.734 ± 0.026	0.3854 ± 0.0023	0.5027 ± 0.0027
2458804.71328670	16.8841 ± 0.0091	0.038 ± 0.007	15.6398	165	0.1067 ± 0.0011	−4.762 ± 0.028	0.3886 ± 0.0023	0.4982 ± 0.0028
2458806.69577168	16.8941 ± 0.0085	0.019 ± 0.007	15.6158	182	0.1052 ± 0.0010	−4.749 ± 0.027	0.3894 ± 0.0022	0.5048 ± 0.0026
2458911.59453852	16.8965 ± 0.0099	0.028 ± 0.008	15.7209	147	0.1047 ± 0.0012	−4.743 ± 0.028	0.3857 ± 0.0027	0.4960 ± 0.0034
2458917.63877563	16.8883 ± 0.0204	0.021 ± 0.013	15.7356	59	0.1110 ± 0.0032	−4.732 ± 0.064	0.3940 ± 0.0069	0.5077 ± 0.0082

Table A2
Radial Velocity and Activity Indices Obtained from the HARPS Spectra

BJD–2457000 (days)	RV (km s^{-1})	Bisector	FWHM	S/N	H_α	$\log(R'_{HK})$	Na II	He I
1464.83460002	16.8822 ± 0.0035	0.015 ± 0.003	14.3788	83	0.1084 ± 0.0008	−4.771 ± 0.029	0.4144 ± 0.0016	0.4977 ± 0.0019
1464.82626718	16.8868 ± 0.0035	0.017 ± 0.003	14.3902	83	0.1071 ± 0.0008	−4.763 ± 0.029	0.4139 ± 0.0016	0.4976 ± 0.0019
1465.80299404	16.9102 ± 0.0020	0.028 ± 0.002	14.3445	118	0.1080 ± 0.0005	−4.714 ± 0.025	0.4111 ± 0.0011	0.4978 ± 0.0013
1465.79547085	16.9147 ± 0.0020	0.025 ± 0.002	14.3513	120	0.1077 ± 0.0005	−4.707 ± 0.025	0.4093 ± 0.0011	0.4973 ± 0.0013
1466.78878939	16.9063 ± 0.0022	0.006 ± 0.002	14.4190	99	0.1079 ± 0.0006	−4.701 ± 0.025	0.4108 ± 0.0013	0.4956 ± 0.0015
1466.79644105	16.9112 ± 0.0020	0.019 ± 0.002	14.4287	107	0.1074 ± 0.0006	−4.675 ± 0.024	0.4131 ± 0.0012	0.4949 ± 0.0014
1481.74528823	16.8882 ± 0.0020	0.024 ± 0.002	14.3635	120	0.1061 ± 0.0006	−4.727 ± 0.026	0.4170 ± 0.0012	0.4979 ± 0.0013
1482.75123537	16.8830 ± 0.0020	0.020 ± 0.002	14.3771	142	0.1062 ± 0.0004	−4.722 ± 0.025	0.4160 ± 0.0009	0.4982 ± 0.0011
1482.74376858	16.8829 ± 0.0020	0.020 ± 0.002	14.3770	145	0.1057 ± 0.0004	−4.740 ± 0.026	0.4159 ± 0.0009	0.4965 ± 0.0011
1483.77055220	16.8847 ± 0.0020	0.009 ± 0.002	14.3640	121	0.1066 ± 0.0005	−4.736 ± 0.026	0.4138 ± 0.0011	0.4978 ± 0.0013
1483.76263412	16.8846 ± 0.0020	0.014 ± 0.002	14.3626	118	0.1067 ± 0.0005	−4.747 ± 0.027	0.4135 ± 0.0011	0.4975 ± 0.0013
1576.54303679	16.9129 ± 0.0029	0.036 ± 0.002	14.3866	90	0.1044 ± 0.0008	−4.894 ± 0.037	0.4165 ± 0.0015	0.4960 ± 0.0018
1762.82961396	16.9229 ± 0.0020	0.014 ± 0.002	14.4052	113	0.1070 ± 0.0006	−4.721 ± 0.026	0.4196 ± 0.0012	0.4996 ± 0.0014
1763.79774196	16.8988 ± 0.0020	0.030 ± 0.002	14.3579	114	0.1061 ± 0.0006	−4.720 ± 0.025	0.4225 ± 0.0012	0.5017 ± 0.0014
1764.83063596	16.9055 ± 0.0020	0.025 ± 0.002	14.3443	139	0.1050 ± 0.0005	−4.751 ± 0.027	0.4237 ± 0.0010	0.5010 ± 0.0012
1773.87633433	16.9275 ± 0.0020	0.014 ± 0.002	14.3624	109	0.1054 ± 0.0006	−4.782 ± 0.029	0.4233 ± 0.0013	0.4989 ± 0.0014
1775.86482034	16.9506 ± 0.0040	0.004 ± 0.003	14.3949	78	0.1056 ± 0.0009	−4.784 ± 0.030	0.4177 ± 0.0017	0.4979 ± 0.0020
1777.74548666	16.9247 ± 0.0083	0.015 ± 0.006	14.3560	52	0.1058 ± 0.0015	−5.023 ± 0.060	0.4254 ± 0.0028	0.4988 ± 0.0031
1803.76107908	16.9097 ± 0.0020	0.032 ± 0.002	14.4174	111	0.1064 ± 0.0006	−4.757 ± 0.027	0.4212 ± 0.0012	0.5007 ± 0.0014
1810.87660156	16.8759 ± 0.0020	0.012 ± 0.002	14.4132	109	0.1054 ± 0.0006	−4.771 ± 0.028	0.4212 ± 0.0012	0.5010 ± 0.0014
1820.86191239	16.9179 ± 0.0020	0.015 ± 0.002	14.3700	114	0.1052 ± 0.0006	−4.766 ± 0.028	0.4167 ± 0.0012	0.5006 ± 0.0013
1831.79439764	16.9347 ± 0.0020	0.029 ± 0.002	14.3699	121	0.1043 ± 0.0006	−4.761 ± 0.028	0.4115 ± 0.0011	0.4982 ± 0.0012
1833.69330017	16.9464 ± 0.0030	0.023 ± 0.002	14.3629	88	0.1040 ± 0.0008	−4.776 ± 0.029	0.4138 ± 0.0015	0.5002 ± 0.0018
1836.70976685	16.9510 ± 0.0020	0.022 ± 0.002	14.3267	107	0.1058 ± 0.0007	−4.757 ± 0.027	0.4183 ± 0.0013	0.4990 ± 0.0015
1839.73047160	16.9502 ± 0.0021	0.021 ± 0.002	14.3294	100	0.1038 ± 0.0007	−4.776 ± 0.029	0.4232 ± 0.0014	0.4998 ± 0.0016
1848.70736633	16.9491 ± 0.0020	0.042 ± 0.002	14.3724	152	0.1045 ± 0.0004	−4.760 ± 0.027	0.4180 ± 0.0009	0.4977 ± 0.0010
1853.82221087	16.9462 ± 0.0020	0.018 ± 0.002	14.3981	106	0.1044 ± 0.0006	−4.748 ± 0.028	0.4055 ± 0.0012	0.4949 ± 0.0014
1855.62240768	16.9285 ± 0.0020	0.011 ± 0.002	14.3667	113	0.1045 ± 0.0006	−4.758 ± 0.027	0.4148 ± 0.0012	0.4974 ± 0.0014
1866.53795150	16.9294 ± 0.0336	0.043 ± 0.025	14.2712	17	0.0828 ± 0.0058	⋯	0.4236 ± 0.0095	0.4839 ± 0.0090
1866.55739621	16.9209 ± 0.0023	0.029 ± 0.002	14.3386	97	0.1031 ± 0.0007	−4.759 ± 0.028	0.4061 ± 0.0014	0.4969 ± 0.0016
1868.53027483	16.9340 ± 0.0020	0.016 ± 0.002	14.3383	116	0.1048 ± 0.0006	−4.761 ± 0.027	0.4005 ± 0.0011	0.4917 ± 0.0013
1875.52489656	16.9384 ± 0.0020	0.020 ± 0.002	14.3597	132	0.1041 ± 0.0005	−4.752 ± 0.027	0.4081 ± 0.0010	0.4947 ± 0.0011
1877.62220328	16.9245 ± 0.0049	0.028 ± 0.004	14.3702	71	0.1015 ± 0.0009	−4.786 ± 0.030	0.4067 ± 0.0017	0.4981 ± 0.0021
1884.61075979	16.9418 ± 0.0056	0.030 ± 0.004	14.3274	66	0.1051 ± 0.0010	−4.792 ± 0.031	0.4170 ± 0.0020	0.4988 ± 0.0023
1886.65333879	16.9538 ± 0.0031	0.027 ± 0.002	14.3517	87	0.1047 ± 0.0007	−4.824 ± 0.032	0.4172 ± 0.0015	0.5010 ± 0.0017
1889.64841759	16.9595 ± 0.0033	0.028 ± 0.002	14.3437	85	0.1050 ± 0.0007	−4.808 ± 0.031	0.4221 ± 0.0015	0.4991 ± 0.0018
1893.71018832	16.9813 ± 0.0020	0.020 ± 0.002	14.3765	104	0.1049 ± 0.0005	−4.804 ± 0.031	0.4128 ± 0.0012	0.4977 ± 0.0013
1896.53584191	16.9733 ± 0.0038	0.024 ± 0.003	14.3444	80	0.1049 ± 0.0008	−4.810 ± 0.031	0.4067 ± 0.0016	0.4951 ± 0.0018
1901.52855834	16.9797 ± 0.0020	0.012 ± 0.002	14.3447	120	0.1043 ± 0.0005	−4.744 ± 0.027	0.4150 ± 0.0011	0.4980 ± 0.0013

Table A3
Radial Velocities Obtained from the CORALIE Spectra

BJD–2457000 (days)	RV (km s^{-1})	FWHM	Contrast	Bisector	Noise	S/N_{10}	S/N_{50}	S/N_{60}
1462.613463	16.830 ± 0.012	14.04027	22.731	−0.01808	0.01151	13.90	43.90	45.80
1473.766468	16.861 ± 0.010	14.00994	22.661	−0.01234	0.00921	19.20	51.10	53.00
1489.763017	16.793 ± 0.017	13.99526	22.967	0.00591	0.01640	9.30	33.10	34.00
1490.818784	16.823 ± 0.015	13.99797	22.900	−0.02211	0.01495	9.80	36.10	37.60
1528.633488	16.889 ± 0.011	14.04580	22.585	−0.03084	0.01032	14.70	48.60	51.10
1533.663477	16.844 ± 0.012	14.02184	22.697	−0.01156	0.01184	14.10	41.90	44.30
1537.619293	16.842 ± 0.011	13.99256	22.683	0.00737	0.01087	15.70	44.40	46.10
1544.675520	16.833 ± 0.012	14.03582	22.648	0.02580	0.01146	13.60	43.90	45.60
1562.609684	16.822 ± 0.015	14.03330	22.664	−0.00991	0.01486	10.30	36.00	37.30
1569.594671	16.838 ± 0.011	14.04995	22.601	−0.01878	0.01042	14.50	47.80	49.30

Table A4
Radial Velocities Obtained from the MINERVA-Australis Spectra

BJD–2457000 (days)	RV (km s^{-1})
1486.154190	−0.020 ± 0.016
1486.168657	0.027 ± 0.014
1486.183125	−0.006 ± 0.014
1494.097685	0.002 ± 0.013
1494.117512	0.027 ± 0.012
1495.176447	0.004 ± 0.012
1495.190914	−0.004 ± 0.012
1496.060648	−0.006 ± 0.013
1496.075104	0.008 ± 0.013
1497.067894	0.019 ± 0.011
1497.082350	−0.020 ± 0.011
1498.078553	0.039 ± 0.013
1498.093021	−0.006 ± 0.013
1499.073831	0.018 ± 0.017
1499.088299	0.032 ± 0.016
1500.058241	0.005 ± 0.014
1500.072708	−0.003 ± 0.012
1501.100590	−0.009 ± 0.013
1501.115046	0.009 ± 0.013
1501.129514	−0.009 ± 0.012
1502.071400	−0.015 ± 0.016
1502.085856	−0.059 ± 0.016
1502.100324	0.019 ± 0.015
1503.098032	−0.021 ± 0.010
1503.119433	−0.009 ± 0.011
1522.930428	0.038 ± 0.016
1527.003877	−0.020 ± 0.024
1529.084062	−0.005 ± 0.017
1529.095058	−0.025 ± 0.019
1531.081898	0.012 ± 0.016
1531.092894	−0.026 ± 0.018
1533.118935	−0.087 ± 0.045
1534.047905	−0.020 ± 0.046
1536.053831	−0.007 ± 0.020
1536.075231	−0.028 ± 0.016
1537.015012	−0.057 ± 0.025
1537.036424	−0.063 ± 0.021
1537.057824	−0.052 ± 0.021
1539.062593	−0.116 ± 0.020
1539.077060	−0.048 ± 0.041
1551.995208	−0.059 ± 0.018
1552.017650	−0.028 ± 0.020
1555.019236	−0.001 ± 0.014
1555.040637	−0.036 ± 0.015
1561.005451	−0.058 ± 0.018
1562.024977	−0.101 ± 0.014
1563.003519	−0.013 ± 0.041
1563.024919	−0.038 ± 0.018
1566.002882	−0.004 ± 0.015
1566.024294	0.002 ± 0.015
1566.953866	0.003 ± 0.013
1566.975278	−0.012 ± 0.014
1574.970301	−0.016 ± 0.020
1574.991701	−0.012 ± 0.017
1576.979456	0.003 ± 0.017
1577.967188	0.016 ± 0.015
1578.968461	−0.023 ± 0.016
1586.017812	−0.001 ± 0.015
1586.981354	−0.034 ± 0.014
1587.002766	0.053 ± 0.016
1587.024167	0.036 ± 0.018
1588.962361	−0.041 ± 0.015

ORCID iDs

Melissa J. Hobson https://orcid.org/0000-0002-5945-7975
Rafael Brahm https://orcid.org/0000-0002-9158-7315
Andrés Jordán https://orcid.org/0000-0002-5389-3944
Nestor Espinoza https://orcid.org/0000-0001-9513-1449
Diana Kossakowski https://orcid.org/0000-0002-0436-7833
Thomas Henning https://orcid.org/0000-0002-1493-300X
Martin Schlecker https://orcid.org/0000-0001-8355-2107
Paula Sarkis https://orcid.org/0000-0001-8128-3126
Trifon Trifonov https://orcid.org/0000-0002-0236-775X
Daniel Thorngren https://orcid.org/0000-0002-5113-8558
Avraham Binnenfeld https://orcid.org/0000-0002-9319-3838
Sahar Shahaf https://orcid.org/0000-0001-9298-8068
Shay Zucker https://orcid.org/0000-0003-3173-3138
George R. Ricker https://orcid.org/0000-0003-2058-6662
David W. Latham https://orcid.org/0000-0001-9911-7388
S. Seager https://orcid.org/0000-0002-6892-6948
Joshua N. Winn https://orcid.org/0000-0002-4265-047X
Jon M. Jenkins https://orcid.org/0000-0002-4715-9460
Brett Addison https://orcid.org/0000-0003-3216-0626
François Bouchy https://orcid.org/0000-0002-7613-393X
Brendan P. Bowler https://orcid.org/0000-0003-2649-2288
Joshua T. Briegal https://orcid.org/0000-0002-7611-8772
Edward M. Bryant https://orcid.org/0000-0001-7904-4441
Karen A. Collins https://orcid.org/0000-0001-6588-9574
Tansu Daylan https://orcid.org/0000-0002-6939-9211
Jonathan Horner https://orcid.org/0000-0002-1160-7970
Chelsea Huang https://orcid.org/0000-0003-0918-7484
Stephen R. Kane https://orcid.org/0000-0002-7084-0529
John Kielkopf https://orcid.org/0000-0003-0497-2651
Brian McLean https://orcid.org/0000-0002-8058-643X
Matthew W. Mengel https://orcid.org/0000-0002-7830-6822
Louise D. Nielsen https://orcid.org/0000-0002-5254-2499
Jack Okumura https://orcid.org/0000-0002-4876-8540
Peter Plavchan https://orcid.org/0000-0002-8864-1667
Avi Shporer https://orcid.org/0000-0002-1836-3120
Alexis M. S. Smith https://orcid.org/0000-0002-2386-4341
C. G. Tinney https://orcid.org/0000-0002-7595-0970
Joseph D. Twicken https://orcid.org/0000-0002-6778-7552
Stéphane Udry https://orcid.org/0000-0001-7576-6236
Robert A. Wittenmyer https://orcid.org/0000-0001-9957-9304

References

Addison, B., Wright, D. J., Wittenmyer, R. A., et al. 2019, PASP, 131, 115003
Addison, B. C., Horner, J., Wittenmyer, R. A., et al. 2020, arXiv:2006.13675
Addison, B. C., Wright, D. J., Nicholson, B. A., et al. 2021, MNRAS, 502, 3704
Baraffe, I., Chabrier, G., & Barman, T. 2008, A&A, 482, 315
Baranne, A., Queloz, D., Mayor, M., et al. 1996, A&AS, 119, 373
Barclay, T., Pepper, J., & Quintana, E. V. 2018, ApJS, 239, 2
Barnes, S. I., Gibson, S., Nield, K., & Cochrane, D. 2012, Proc. SPIE, 8446, 844688
Binnenfeld, A., Shahaf, S., & Zucker, S. 2020, A&A, 642, A146
Boisse, I., Moutou, C., Vidal-Madjar, A., et al. 2009, A&A, 495, 959
Brahm, R., Espinoza, N., Jordán, A., et al. 2019, AJ, 158, 45
Brahm, R., Jordán, A., & Espinoza, N. 2017a, PASP, 129, 034002
Brahm, R., Jordán, A., Hartman, J., & Bakos, G. 2017b, MNRAS, 467, 971
Bressan, A., Marigo, P., Girardi, L., et al. 2012, MNRAS, 427, 127
Brown, T. M., Baliber, N., Bianco, F. B., et al. 2013, PASP, 125, 1031

Bruno, G., Almenara, J. M., Barros, S. C. C., et al. 2015, A&A, 573, A124
Bryant, E. M., Bayliss, D., McCormac, J., et al. 2020, MNRAS, 494, 5872
Buchner, J., Georgakakis, A., Nandra, K., et al. 2014, A&A, 564, A125
Canto Martins, B. L., Gomes, R. L., Messias, Y. S., et al. 2020, ApJS, 250, 20
Castelli, F., & Kurucz, R. L. 2003, in IAU Symp. 210, Modelling of Stellar Atmospheres, ed. N. Piskunov, W. W. Weiss, & D. F. Gray (San Fransisco, CA: ASP), A20
David, T. J., Contardo, G., Sandoval, A., et al. 2011, arXiv:2011.09894
Dawson, R. I., & Johnson, J. A. 2018, ARA&A, 56, 175
Duncan, D. K., Vaughan, A. H., Wilson, O. C., et al. 1991, ApJS, 76, 383
Espinoza, N. 2018, RNAAS, 2, 209
Espinoza, N., Kossakowski, D., & Brahm, R. 2019, MNRAS, 490, 2262
Feroz, F., Hobson, M. P., & Bridges, M. 2009, MNRAS, 398, 1601
Foreman-Mackey, D., Agol, E., Ambikasaran, S., & Angus, R. 2017, AJ, 154, 220
Foreman-Mackey, D., Hogg, D. W., Lang, D., & Goodman, J. 2013, PASP, 125, 306
Fulton, B. J., Petigura, E. A., Blunt, S., & Sinukoff, E. 2018, PASP, 130, 044504
Gaia Collaboration, Brown, A. G. A., Vallenari, A., et al. 2018, A&A, 616, A1
Gaia Collaboration, Prusti, T., de Bruijne, J. H. J., et al. 2016, A&A, 595, A1
Gomes da Silva, J., Santos, N. C., Bonfils, X., et al. 2011, A&A, 534, A30
Jenkins, J. M. 2002, ApJ, 575, 493
Jenkins, J. M., Chandrasekaran, H., McCauliff, S. D., et al. 2010, Proc. SPIE, 7740, 77400D
Jenkins, J. M., Tenenbaum, P., Seader, S., et al. 2020, Kepler Data Processing Handbook: Transiting Planet Search, Kepler Science Document KSCI-19081-003
Jenkins, J. M., Twicken, J. D., McCauliff, S., et al. 2016, Proc. SPIE, 9913, 99133E
Jordán, A., Brahm, R., Espinoza, N., et al. 2020, AJ, 159, 145
Kaufer, A., Stahl, O., Tubbesing, S., et al. 1999, Msngr, 95, 8
Kreidberg, L. 2015, PASP, 127, 1161
Li, J., Tenenbaum, P., Twicken, J. D., et al. 2019, PASP, 131, 024506
Mayor, M., Pepe, F., Queloz, D., et al. 2003, Msngr, 114, 20
McLaughlin, D. B. 1924, ApJ, 60, 22
Méndez, A., & Rivera-Valentín, E. G. 2017, ApJL, 837, L1
Mordasini, C., Alibert, Y., Georgy, C., et al. 2012a, A&A, 547, A112
Mordasini, C., Alibert, Y., Klahr, H., & Henning, T. 2012b, A&A, 547, A111
Müller, S., Ben-Yami, M., & Helled, R. 2020, ApJ, 903, 147
Munari, U., Henden, A., Frigo, A., et al. 2014, AJ, 148, 81
Noyes, R. W., Hartmann, L. W., Baliunas, S. L., Duncan, D. K., & Vaughan, A. H. 1984, ApJ, 279, 763
Otegi, J. F., Bouchy, F., & Helled, R. 2020, A&A, 634, A43
Panichi, F., Goździewski, K., Migaszewski, C., & Szuszkiewicz, E. 2018, MNRAS, 478, 2480
Pecaut, M. J., & Mamajek, E. E. 2013, ApJS, 208, 9
Pepe, F., Mayor, M., Rupprecht, G., et al. 2002, Msngr, 110, 9
Queloz, D., Henry, G. W., Sivan, J. P., et al. 2001a, A&A, 379, 279
Queloz, D., Mayor, M., Udry, S., et al. 2001b, Msngr, 105, 1
Ricker, G. R., Winn, J. N., Vanderspek, R., et al. 2015, JATIS, 1, 014003
Rossiter, R. A. 1924, ApJ, 60, 15
Sarkis, P., Mordasini, C., Henning, T., Marleau, G. D., & Mollière, P. 2021, A&A, 645, A79
Shahaf, S., Binnenfeld, A., Mazeh, T., & Zucker, S. 2020, SPARTA: SPectroscopic vARiabiliTy Analysis, Astrophysics Source Code Library, ascl:2007.022
Siverd, R. J., Brown, T. M., Barnes, S., et al. 2018, Proc. SPIE, 10702, 107026C
Skrutskie, M. F., Cutri, R. M., Stiening, R., et al. 2006, AJ, 131, 1163
Smith, J. C., Stumpe, M. C., Van Cleve, J. E., et al. 2012, PASP, 124, 1000
Southworth, J. 2011, MNRAS, 417, 2166
Speagle, J. S. 2020, MNRAS, 493, 3132
Stassun, K. G. 2019, yCat, 4038, 0
Stumpe, M. C., Smith, J. C., Catanzarite, J. H., et al. 2014, PASP, 126, 100
Stumpe, M. C., Smith, J. C., Van Cleve, J. E., et al. 2012, PASP, 124, 985
Sullivan, P. W., Winn, J. N., Berta-Thompson, Z. K., et al. 2015, ApJ, 809, 77
Thorngren, D., & Fortney, J. J. 2019, ApJL, 874, L31
Tokovinin, A. 2018, PASP, 130, 035002
Triaud, A. H. M. J. 2018, in Handbook of Exoplanets, ed. H. Deeg & J. Belmonte (Cham: Springer), 2
Twicken, J. D., Catanzarite, J. H., Clarke, B. D., et al. 2018, PASP, 130, 064502
Wheatley, P. J., West, R. G., Goad, M. R., et al. 2018, MNRAS, 475, 4476
Winn, J. N. 2010, in Exoplanets, ed. S. Seager (Tucson, AZ: Univ. Arizona Press), 55
Yee, S. W., Petigura, E. A., & von Braun, K. 2017, ApJ, 836, 77
Ziegler, C., Tokovinin, A., Briceño, C., et al. 2020, AJ, 159, 19
Zucker, S. 2018, MNRAS, 474, L86